FERMILAB-Pub-04/090-E July 2004

Test of 2000 Phototubes for the CDF Endplug Calorimeter Upgrade

L. Breccia [a], S.W. Delchamps [b,1] , I. Fiori [a,2] , G. Farinelli [a], J. Freeman [b], T. Jaffrey [b],
W. Kinney [b], W. Koska [b,3] , P. Limon [b], M. Mishina [b,*], G. Pauletta [c], J. Strait [b],
S. Zucchelli [a]

[a] *Istituto Nazionale di Fisica Nucleare, University of Bologna, 40127 Bologna, Italy*
[b] *Fermi National Accelerator Laboratory, Batavia, Illinois 60510, USA*
[c] *Istituto Nazionale di Fisica Nucleare, University of Udine, Udine, Italy*

Abstract

Over 2,000 photomultiplier tubes have been selected as the readout device of the upgrade CDF Endplug calorimeter, a scintillator tile sampling calorimeter with wave-shifter fiber readout. The specifications were set on various properties of the tubes for the electromagnetic and hadronic compartments and a series of rigorous tests were made on 2,216 Hamamatsu R4125, 10-stage 19 mm diameter tubes with green-extended bialkali photocathode. On all of the test items, the distributions of the data were well clustered with minor tails, and the original specifications based on a small ensemble were well suited for rejecting the tails of the distributions. After rejecting 5.4 % of the total, 960 tubes for electromagnetic and 864 tubes for hadronic compartments were allocated to projective towers based on their linear dynamic ranges. Tubes with greater linear ranges were assigned to larger pseudo- rapidity channels where greater single-tower energy deposits were expected. This paper describes how we selected the phototubes for our calorimeter and presents the results of the study we made.

Key words: phototube, calorimeter, collider, high energy physics
PACS: 85.60.Ha, 29.40.Mc, 29.40.Vj

---

1. Introduction

The photomultiplier tube has been one of the most reliable elements of particle detectors as exemplified by our experience on the CDF Central and Wall Calorimeters[1,2], and it has evolved from a less demanding discrete pulse counter towards a precise pulse height measuring device. Scintillator-based calorimeters for collider experiments and Cerenkov light detectors in astrophysics experiments are typical examples. These applications

---

[*] corresponding author:
Email address: mishina@fnal.gov. Address:Fermilab, P.O. Box 500, Batavia, IL 60510. USA. Tel: (630)840-4603. (M. Mishina).

[1] Present address: Northern Illinois University, Dekalb, Illinois,USA

[2] Present address; Universita di Padova, INFN, 35131 Padova, Italy

[3] Present address:Lucent Technologies, Lombard, Illinois USA

- have a large number of phototubes;
- are in a semi-permanent setup;
- have limited accessibility;
- are for a long-term experiment;
- measure the pulse height accurately;
- require large dynamic range.

In these applications, long term stability is a far more stringent requirement than in discrete pulse counting devices.

In this report, we present the results of our detailed studies on the qualities of the phototubes we have selected for our newly commissioned CDF endplug calorimeter. A total of 2,216 phototubes were subjected to screening based on a set of predetermined specifications.

1.1. *CDF upgrade for RUN II*

CDF has recently completed an extensive upgrade of its detector systems[3] towards the high luminosity run, Run II started in 2001.

The upgrade was to achieve full data taking capability in the new collider environment of the significantly upgraded Tevatron accelerator complex[4] which has been strengthened by the newly commissioned 150-GeV Main Injector. The 8-GeV Booster and the Anti-Proton Source have also been much improved in intensity. These all combined, we would expect a much higher luminosity compared to the previous run, Run I. The basic run conditions assumed for Run II are shown in Table 1.

E_{cms}	1.96 TeV
Max instantaneous luminosity	1 (2)$\times 10^{32} cm^{-2} s^{-1}$
Beam bunch crossing interval	396 (132) ns
Total integrated luminosity	2 (15) fb^{-1}

Table 1
Condition of Run II. The numbers in parentheses are the parameters in the second phase, Run IIb.

The most significant change is the beam crossing interval which has been shortened by almost an order of magnitude from the previous 3.5 μ sec in the first phase and will be further shortened in the second phase. Also the increase of the c.m.s. energy from 1.8 TeV to 1.96 TeV will in general increase the cross sections. Therefore all the components with slow time constants in the original CDF system have been replaced.

1.2. *Endplug calorimeter upgrade*

The two Endplug calorimeter modules[3] are among the components reconstructed under the upgrade program. The original calorimeters in the forward-backward region, "Endplug"[5] and "Forward"[6] were based on proportional tubes as the sampling media whose signal time constant would no longer match the new environment.

The basic requirements for the original calorimeters in the forward-backward region;
- fine granularity in lateral segmentation;
- projective tower geometry;
- two longitudinal compartments, electromagnetic and hadronic;
- hermeticity in energy flow measurement;
- uniformity in response across the lateral span;

would remain to be met by the new calorimeter.

After a wide range of search for a possible alternative technology, we chose the tile-fiber sampling technique[7,8] as a plausible solution and then a significant effort went into R&D[9] to bring the technology to the level that satisfy the above requirements.

In order to preserve the overall geometry and hence the solenoidal field unchanged, the new Endplug calorimeter has kept the original steel structure; 16 steel plates as the return yoke for the solenoid serving also as the absorber plates for the hadronic (HAD) compartment of the calorimeter. The sampling media, however, were replaced by plastic scintillator tiles with wave-length-shifter (WLS) fiber readout to achieve fast time response appropriate for the new beam crossing cycle.

In addition to the faster time response, the physical thickness of the scintillator sampling layers is much smaller than the original gas sampling layers. Therefore we were able to implement a total of 23 layers (20 X_0 and 1.0 λ_{int}) of lead-scintillator sandwiches as the electromagnetic (EM) compartment, still leaving enough space for four additional HAD layers in front of the original steel plate structure. Thus, a total of 22 layers (7.0 λ_{int}) of steel-scintillator sandwiches was implemented as the hadronic compartment without changing the original overall depth. These four additional layers were made of stainless steel plates so that the solenoidal field was not altered. Furthermore, the opening of the Endplug in the forward and backward direction along the beam axis was closed down to 3° in polar angle, θ, (sampling down to 3.5°, 3.5 in pseudo-rapidity. η) from the original 10°. Again, the extended portion of the steel absorber plates between 3° and 10° are made of stainless steel. By this extension, the original Forward calorimeters that used to cover the forward-backward angles below 10° have been removed, eliminating the discontinuities at boundaries. Subsequently the forward-backward muon systems were moved to the position immediately outside of the Endplug calorimeter to improve the coverage around 30°. The upper half of the $r - z$ cross-sectional view of one of the new Endplug calorimeters is shown in Fig. 1.

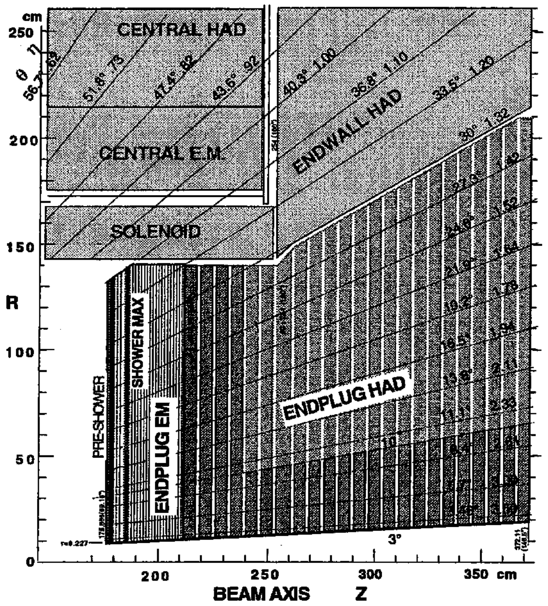

Fig. 1. $r - z$ cross-sectional view of the upgraded Endplug Calorimeter of CDF. Slightly darker shade in HAD compartment signifies the newly added portion made of stainless steel.

1.3. *Longitudinal layer configuration*

The EM compartment is made of 23 layers of 5.5 mm thick calcium-loaded lead sheets (0.3 mm thick stainless steel cladding on both surfaces) interleaved with plastic scintillator layers. The first layer, immediately behind the structural cover plate, is a Preshower Detector[10] and the fifth layer shares the gap behind the absorber with an independent Shower Maximum Detector[11] both of which are connected to separate phototubes. The total of 22 layers from the second layer on compose the projective towers which are each connected to a single phototube. The corresponding projective towers of the 22-layer HAD compartment are each connected to a separate phototube. These phototubes are the subject of this study. Each layer is a flat assembly of tiles [12,13] made of Kuraray SCSN-38, blue cross-linked polystyrene scintillator[14], 4-mm thick for EM and 6-mm for HAD.

The longitudinal configuration of the EM layers is summarized in Table 2.

Front Cover	: Stainless steel plate (12.7 mm)
Layer 1	: Preshower Detector Bicron BC-408 PVT scintillator tiles (10 mm)
Layers 2 ∼ 23	: Normal sampling layer Pb absorber (4.5 mm) s.s. clad. (0.45 mm) front & back Kuraray SCSN-38 Polystyrene scintillator tiles (4 mm)
Layer 5	: Shower Maximum Detector Bicron BC-404 PVT scintillator strips (6 mm) 2 layers

Table 2
E.M. layer configuration. Longitudinal thicknesses are denoted in parentheses.

The configuration of the HAD compartment is summarized in Table 3.

Layers 1 ~ 22 : Normal sampling layer
Steel absorber (50.8 mm except layer 6 of 63.5 mm)
Kuraray SCSN-38 Polystyrene scintil. (6 mm)

Table 3
HAD layer configuration. Longitudinal thicknesses are denoted in parentheses.

1.4. *Projective towers and tile-fiber readout*

1.4.1. *Scintillator tile assembly and optical connection*

As in the original system, the new Endplug calorimeter is laterally segmented into projective towers. The tiles for EM and HAD were segmented in a common projective tower geometry. A sketch of the lateral view of a mechanical unit of $\Delta\phi = 15°$ of EM is schematically shown in Fig. 2. The mechanical package for the HAD tiles is 30° in ϕ. Each of the fan-shaped scintillator tiles corresponding to each of the projective towers was read out by a WLS fiber, as shown in the inset of Fig. 2. The WLS fiber is a 0.835 mm diameter Kuraray Y-11, a double-clad polystyrene-core fiber with green fluor. The WLS fiber is embedded in a keyhole-shaped groove engraved along the perimeter of the surface of the tile. The WLS fiber encircles the tile with one end mirrored by aluminum sputtering and the other end spliced to a clear fiber of the same diameter at the end of one full turn. The clear fibers from the tiles are brought to the edge of a "pizza pan", a flat assembly of tiles 15° (30°) for EM (HAD) in ϕ with a plastic backing panel, in each layer and connected to an optical fiber cable via a multi-fiber connector[15]. The cable is a flat ribbon of ten clear, double-clad, polystyrene core fibers of 0.9 mm diameter.

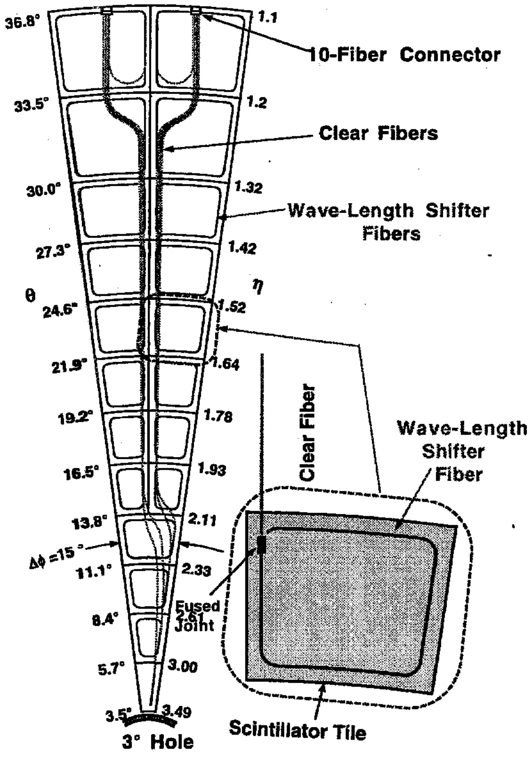

Fig. 2. Lateral segmentation of the scintillator tiles in projective tower geometry.

Optical cables are strung through a gap at a polar angle of 30° over the surface of the conical envelop of the Endplug structure to the rear end of the Endplug and are rearranged from layer-by-layer bundles into projective-tower unit bundles. Thus 21 (22) fibers from an EM (HAD) projective tower are viewed by a single phototube through a square rod of Plexiglass light mixer. The profile of the light mixer (14.5 mm diagonal) is slightly smaller than the sensitive area of the photocathode (15 mm min. in diam.) of the chosen phototube. (See Section 2.6.)

	Lateral Segmentation $N_\eta \times N_\phi$	
	EM	*HAD*
	$1.1 \leqq \eta \leqq 3.49$	$1.32 \leqq \eta \leqq 3.49$
$\eta \leqq 2.11$ ($\Delta\phi = 7.5°$)	8 × 48	7 × 48
$\eta \geqq 2.11$ ($\Delta\phi = 15°$)	4 × 24	4 × 24
No. of Tubes :		
East or West	480	432
East + West	960	864

Table 4
Lateral segmentation and number of phototubes

The lateral segmentation shown in Fig. 2 results in a total of 960 tubes for EM and 864 tubes for

HAD, as listed in Table. 4.

In addition, a Y-11 WLS fiber is brought to each tube as a monitoring light source. The WLS fiber is illuminated by a block of scintillator of the same material as the scintillator tiles, blue SCSN-38, which in turn is excited by UV light (337 nm) transmitted by a quartz fiber from a pulsed nitrogen laser[16]. Fig. 3 is a sketch of the phototube assembly.

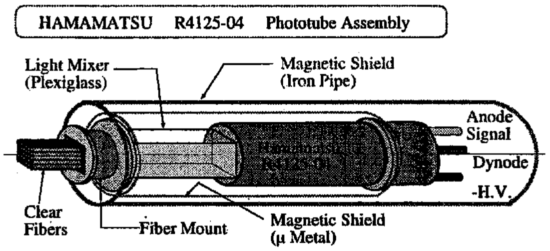

Fig. 3. Sketch of the phototube assembly. (Not to scale.)

The dimensions of the components in the phototube assembly is shown in Table 5.

Iron Pipe	3.6 mm Wall, 35 mm ID, 214 mm L
μ-Metal tube	1 mm Wall, 25.4 mm ID, 140 mm L
Light Mixer	$(10.3mm)^2$, 58 mm L
PMT glass envelop	18.6 mm OD, 88 mm L

Table 5
Dimensions of the components in PMT assembly.

1.4.2. *Magnetic shield*

Since the steel plates of the HAD compartment is a part of the flux return path of the solenoid, stray magnetic field on the rear surface of the Endplug structure where the phototube housings were to be mounted needed some attention. A measurement showed that the maximum of the stray field was about 200 Gauss[17] at around the conical crack at $\theta = 30°$ and less than 50 Gauss at lower angles where the phototube housing would be located.

In the phototube assembly shown in Fig. 3, shielding against magnetic field is provided by a 1-mm thick μ-Metal inner tube and a 3.6-mm thick soft iron outer tube. The μ-Metal tube is covering the phototube from the end of the glass stem to 5 *cm* beyond the front face and the outer iron pipe is extending beyond the μ-Metal tube by 6 (1) cm at the front (rear) end.

Tests were conducted with such assembly in a magnetic field[18]. The phototube was kept at a low relative gain (See Section 5.1.1 for the definition.) of 5×10^4 to be sensitive to the magnetic field. It was found that there was little change ($< 1\%$) in the response up to 170 (220) Gauss for the field parallel (perpendicular) to the axis of the phototube. Therefore it was concluded that the magnetic shield would be quite adequate for the measured level of the stray field.

1.4.3. *Spectral matching of optical components*

The scintillator for the tiles, Kuraray SCSN-38, is a fast and efficient blue polystyrene scintillator with a peak emission at 428 nm[14]. Green-light emitting Y-11 was chosen for its excellent wave-length shifting efficiency with its absorption band well matched to the emission band of SCSN-38. Also important is its emission band peaking at 476 nm with an extended tail beyond 500 nm which gives a good transmission through rather long, up to ~3 *meter*, clear fiber. The green emission band is also important in ensuring tolerance against long term exposure to radiation at these forward angles. However, the green emission band of the WLS fiber severely constrains the type of photocathode of the phototubes. The response of an ordinary bialkali photocathode falls off rapidly beyond ~450 *nm* and the only practical choice is a so-called extended bialkali photocathode which has quantum efficiency of ~12 % at 480 nm. This was one of the major considerations for choosing the phototubes for our purpose.

1.5. *Selection process*

In order to select a total of 1,824 phototubes, 960 for the EM towers, 864 for HAD towers, and spares of about 10 % of the total, we have set criteria based on physics requirements and tested a small number of samples from five different manufacturers. Based on the findings from the samples, we have selected Hamamatsu 4125-04. Then we established a set of specifications, and developed a systematic procedure to test the tubes. We have tested a total of 2,216 tubes, selected those that satisfied the criteria, and allocated them to the projective towers based on their linear dynamic range, so that the tubes of higher dynamic range were allocated to larger η towers where higher energy particles would hit. The tubes were delivered from December 1993 through April 1995. The test on 32 tubes at a time normally took about a week and in some cases the test was repeated if some irregularities were found in the data. The initial test was carried out within a year after the delivery and the final test took place in a period of three years between March 1995 and March 1998. Therefore the final test was performed an average of 26 months, 6 months at the earliest and 46 months at the latest, after the delivery from the manufacturer.

2. Specifications

2.1. *General requirements*

There are generic requirements for the phototubes such as:

- low noise;
- stability in time;
- limited range of the tube-to-tube variation of the operating voltage for a given gain;
- linearity within the required dynamic range.

In addition, there are specific requirements for the desired performance under our expected experimental conditions. The electrical requirements and the corresponding experimental conditions are:

- dynamic range:
  from minimum ionizing particles up to the maximum energy deposit in a single tower.
- stability against background current fluctuation:
  due to fluctuating energy deposit into each tower including the effect of multiple minimum bias events in each bunch crossing.
- lifetime in terms of total accumulated charge:
  to sustain the total accumulated luminosity over the entire run.

These requirements were subsequently converted into electrical specifications once the overall optical system response and the gain of the tubes, including the quantum efficiency, were determined.

2.2. *Maximum energy deposit*

The expected maximum energy per tower was estimated using the Run I[19] data. The data of the energy deposit by inclusive jet events in the projective towers in the forward angles was extrapolated to the Run II conditions of the the c.m.s. energy and the the total integrated luminosity. Given the fact that the transverse momentum distribution of the particles from minimum bias events is flat in η, the average energy of the background particles increases with the η of the towers. However, the smallest polar angle towers with small physical aperture in azimuth do not fully contain a shower, even a narrow profile EM shower. Therefore the maximum energy deposit is expected to be several hundred GeV in the towers at η from 2 to 2.5.

2.3. *Linear dynamic range*

A minimum ionizing particle (MIP) is expected to generate a signal equivalent to a $\sim$0.3 *GeV* EM shower[4]. Therefore we need to have a dynamic range of about 1600 between a MIP and a $\sim$500 *GeV* EM shower. A beam test of prototype modules[21,22] later confirmed this ratio. A study[23] showed about 6 photo-electrons (p.e.) per tile per MIP[5] giving $\sim$120 p.e.'s as the total light output from EM. The quantum efficiency of the phototube is expected to be about 12 % in the green ($\sim$480 *nm*) region, so a fairly large gain is desirable in order to measure a MIP cleanly. However, considering the large dynamic range to be covered, we have limited the gain to $\sim 10^4$ for the tubes in the EM towers and to $\sim 10^5$ in the

---

[4] A MIP loses a total of $\sim$220 *MeV* in the material listed in Table 2 which is scaled by $1/0.7 \sim 1/0.6$[20] into the equivalent electron energy.

[5] The number of p.e. was later confirmed to be $5.6 \sim 5.8$ in a cosmic ray test of all EM layers[10,21].

HAD towers. The dynamic range of the front-end ADC[3,19,24] was subsequently determined.

2.4. *Background current*

The expected average number of minimum bias events is six in a single beam bunch crossing, which causes significant background current. Considering that the two towers of the largest η do not fully contain showers and that they are not covered by the tracking system, 1 μA was taken as a practical maximum for the background current[23].

2.5. *Lifetime*

The lifetime can be usefully defined in terms of the total charge drained from the anode that results in a 15 % gain decrease[25]. The lifetime of the tube we selected, Hamamatsu R4125, was measured to be ~100 *Coulomb*. This corresponds to continuously drawing 3 μA for one full calendar year ($\sim\pi\cdot10^7$ s), and considering the beam running duty factor, we judged that there is sufficient tube life for the Runs II *a* and *b* for the essential parts of the calorimeter.

2.6. *Choice of the phototube*

The spectrum of the light output from WLS fiber dictates that the photocathode must be bialkali type (See Section 1.4.3).

The diameter needs to be large enough to view the bundle of 23 fibers via a light mixer rod, but is restricted by the available space for mounting on the outside surface of the Endplug calorimeter structure. We determined 19 mm diameter tubes to be satisfactory.

To achieve a linear dynamic range of a factor of 1600 at a gain of $\sim10^4(\sim10^5)$ for EM (HAD), eight or ten stage tubes were considered to be adequate.

With regard to these requirements we have tested samples of phototubes from five different manufacturers[25]. Tests were made on :

- relative quantum efficiency;
- uniformity of the response over the surface area;
- gain vs. voltage;
- linear dynamic range;
- noise current;
- stability in time;
- stability against background current fluctuation;
- stability against turning high voltage on and off;
- life in terms of total accumulated charge.

After these tests, we chose Hamamatsu R4125-04 whose specifications are listed in Table 6.

Number of stages	: 10
Photocathode material	: green-extended bialkali
Sensitive area	: 15 mm diameter (min)
Outer diameter	: 18.6±0.7 mm
Length (Glass envelope)	: 88±2 mm
Quantum efficiency at peak	: 27 %
at 480 nm	: ~12 %

Table 6
Physical specifications of the Hamamatsu R-4125-04

2.7. *Phototube base*

The base is a resistor chain type, draining 500 μA to sustain normal response against a possible background current of 1 μA. The circuit diagram is shown in Fig. 4.

The voltage distribution in the above figure is:

$$\begin{array}{cccccccccccccc} K & & D_1 & & D_2 \ldots\ldots\ldots D_7 & & D_8 & & D_9 & & D_{10} & & A \\ 2 & : & 1 & : & \ldots\ldots\ldots & : & 1 & : & 2 & : & 4 & : & 3. \end{array}$$

While the voltages across the middle stage dynodes are the same, the voltage between the cathode and the first dynode is doubled to ensure high electron collection efficiency. The voltages across the last three dynodes are tapered to provide good linearity for large pulses. The signal from the last dynode is picked off for timing purpose which is useful in rejecting cosmic ray background. The heat dissipation is kept under 1 W. The base packages were assembled by Thorn EMI Corporation and tested at Fermilab.

2.8. *Final specification*

We then made a list of specifications stringent enough for our purpose but still practical so that

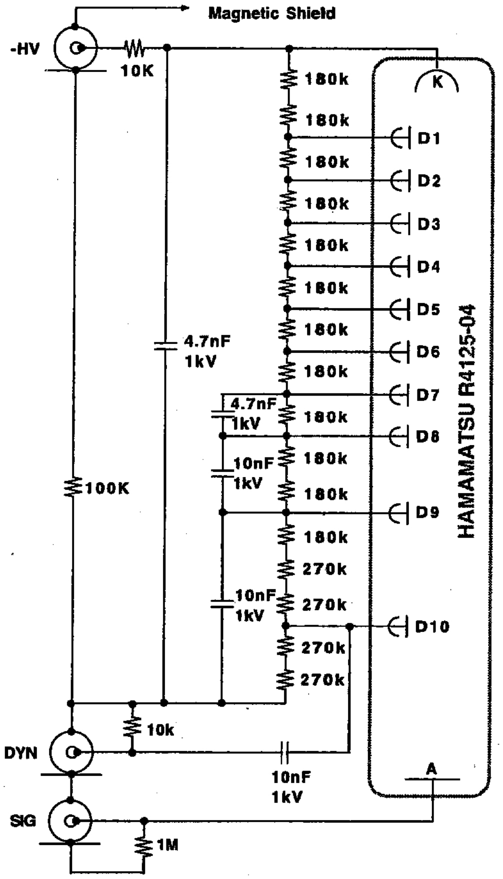

Fig. 4. Circuit diagram of the phototube base.

a large fraction of the tubes would not be rejected. The allowable range of the parameters was established by a series of tests made on a small number of samples as described in [25]. The performance specifications of the tube are shown in Table 7.

How these quantities are measured is described in Section 5.

Quantum eff. at 480 nm	≥ 12 %
Photocathode uniformity	≥ 80 %
Relative Gain G'	EM: $\approx 10^4$ HAD: $\approx 10^5$
Spread of operating voltage	≤ 20 % at G' = 5×10^5
Maximum peak current within 2 % from linearity	≥ 10 mA at G' = 1×10^4 ≥ 20 mA at G' = 5×10^4 ≥ 35 mA at G' = 1×10^5 ≥ 70 mA at G' = 5×10^5
Dark current	≤ 5 nA at G' = 5×10^5
Drift of response in time	≤ 6 % in 48 hours
Shift of response for Bkg current change of 1 μA	≤ 5 %

Table 7
Performance specifications of the tube. The definition of the quantities listed above are explained in section 5.

3. Data provided by the manufacturer

All the tubes were subjected to an initial aging process[26] after assembly at the manufacturer, Hamamatsu Photonics. Each tube was held at 900 Volts and illuminated by a tungsten lamp over the entire photocathode surface. The light intensity was adjusted to draw a sustained anode current of 200 μA. This treatment was continued for about 18 hours.

The tubes were delivered with a data sheet of the following four quantities measured on each of the tubes after the above aging process:

- cathode luminous sensitivity;
- cathode blue sensitivity;
- voltage for nominal gain 5×10^5;
- dark current for nominal gain 5×10^5.

All these quantities are DC current measurement at the photocathode and the anode[26,27]. The distributions of these four quantities are shown in Fig. 5.

In the manufacturer's measurement of the voltage for the nominal gain of 5×10^5, the base voltage distribution was the same as our base assembly (Section 2.7) and the gain was defined as the ratio between the anode output current and the cathode input current.

It is evident from Fig. 5*d* that the tail of the dark current distribution beyond 5 nA was trimmed by selection to comply with our specification. There is a clear proportionality, as shown in the scatter plot in Fig. 6, between the cathode blue sensitivity and the luminous sensitivity, as expected. The linear

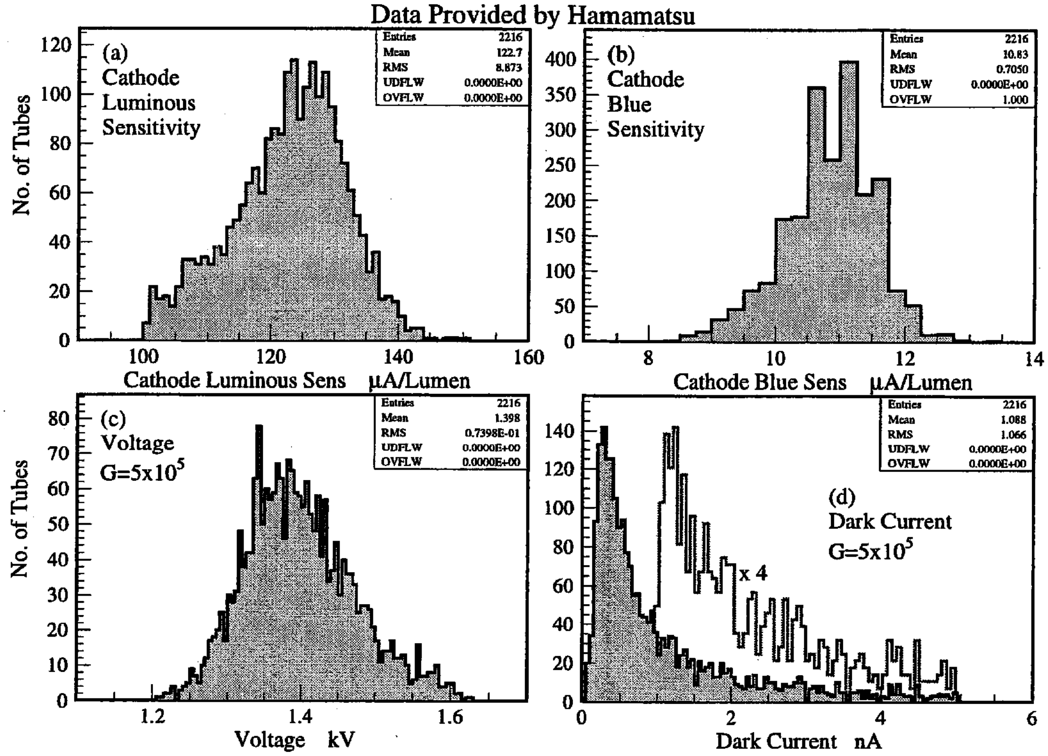

Fig. 5. Histograms of the data provided by Hamamatsu. (a) Cathode luminous sensitivity. (b) Cathode blue sensitivity. (c) Voltage for the nominal gain of 5×10^5. (d) Dark current at the nominal gain of 5×10^5. The portion of $\geq$ 1 nA is superimposed with an enlarged scale.

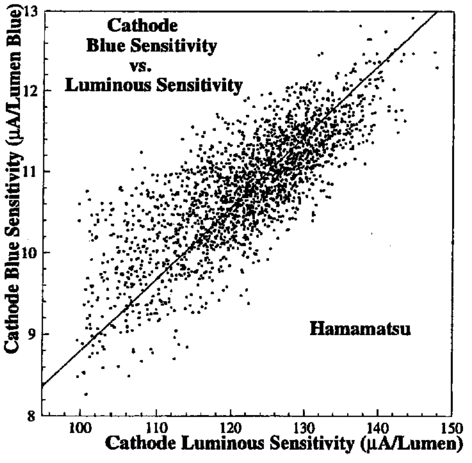

Fig. 6. Scatter plot of cathode blue sensitivity against cathode luminous sensitivity. The line is the straight line fit to the distribution.

fit to the distribution is shown in the figure.

Other scatter plots between these four quantities do not exhibit visible correlations beyond the spread of the data points.

Though the cathode luminous sensitivity and the cathode blue sensitivity are measured each with specific light source[27], it must have some relevance to the quantum efficiency.

We will compare these data with the results of our own measurement in Section 5.

4. Test procedure and setup

In the following sections, we describe the test procedure, the test setup, and the data acquisition system.

4.1. *Test procedure*

A total of 2216 Hamamatsu R4125-04 tubes were delivered from the manufacturer which we subjected to a series of tests (initial test, hereafter) at Fermilab. After the initial test, all tubes went through a conditioning process and then another series of tests (final test, hereafter). The final test was conducted at two sites, Fermilab for about 1300 tubes and INFN Bologna for the rest. The tests were carried out semi-automatically by a host computer at each site running a program developed independently.

The sequence of the test is illustrated in the flow chart shown in Fig. 7.

Prior to the initial test, every tube was visually inspected to detect any apparent problems such as cracks developed during shipment.

At this point, every tube was mounted permanently in an assembly previously shown in Fig. 3(section 1.4.1) without the receptacle for the incoming optical fibers. The subsequent tests were all performed on such assemblies.

In the initial test, the first was a qualitative check of the output signal on an oscilloscope with 1.7 kV applied. Obvious problems such as absence of the signal due to lost vacuum caused by undetected cracks are found at this point. The first of the quantitative tests was the measurement of the relative gain as a function of the voltage, including a measurement of the dark current. After the gain-voltage relationship was established, a stability test was made.

After this initial test, all tubes underwent a conditioning process in which the tubes were exposed to steady LED light at a sustained anode current of 2 μA at a relative gain of 5×10^5 for 48 hours.

After conditioning, the final test repeated the measurement of gain-voltage relationship, dark current, and stability test. Response to turning the high voltage on and off was also measured. Then the linear dynamic range was tested at four different gains. As a check of the consistency of the photocathode quality, the relative quantum efficiency was measured for a small number of tubes sampled from each delivery batch.

The test items for the initial test are summarized in the following list:

(a) gain vs. voltage relationship;
(b) dark current;
(c) stability after turning on high voltage;
(d) stability against background current change.

The test items for the final test are:

(a) gain vs. voltage relationship;
(b) dark current;
(c) linearity;
(d) stability in time after turning on the high voltage;
(e) stability against background current change;
(f) relative quantum efficiency for a sample of tubes from each batch.

The tests that did not require voltage scanning were all conducted at a relative gain of 5×10^5.

4.2. *Test setup*

We have built two nearly identical test setups, one at Fermilab and another at INFN Bologna. The block diagram of the test setup at the Bologna site is shown in Fig. 8.

4.2.1. *Phototube test enclosure*

As shown in Fig. 8, the enclosure of the setup to test 32 tubes at a time was partitioned into two light tight compartments, one for the tubes and the other for light sources.

There were three types of light sources; a block of blue scintillator illuminating 32 short Y-11 WLS fibers, an array of 32 green LED's, and an array of 32 red LED's. Clear polystyrene-core fibers were routed through the partition to connect the tubes and the light sources optically; three fibers per tube, one each for each of the three light sources. The ends of the three clear fibers per tube were attached to the front face of a Plexiglass light mixer. The tube to be tested was mounted behind the light mixer with the same geometry as the final assembly illustrated in Fig. 3.

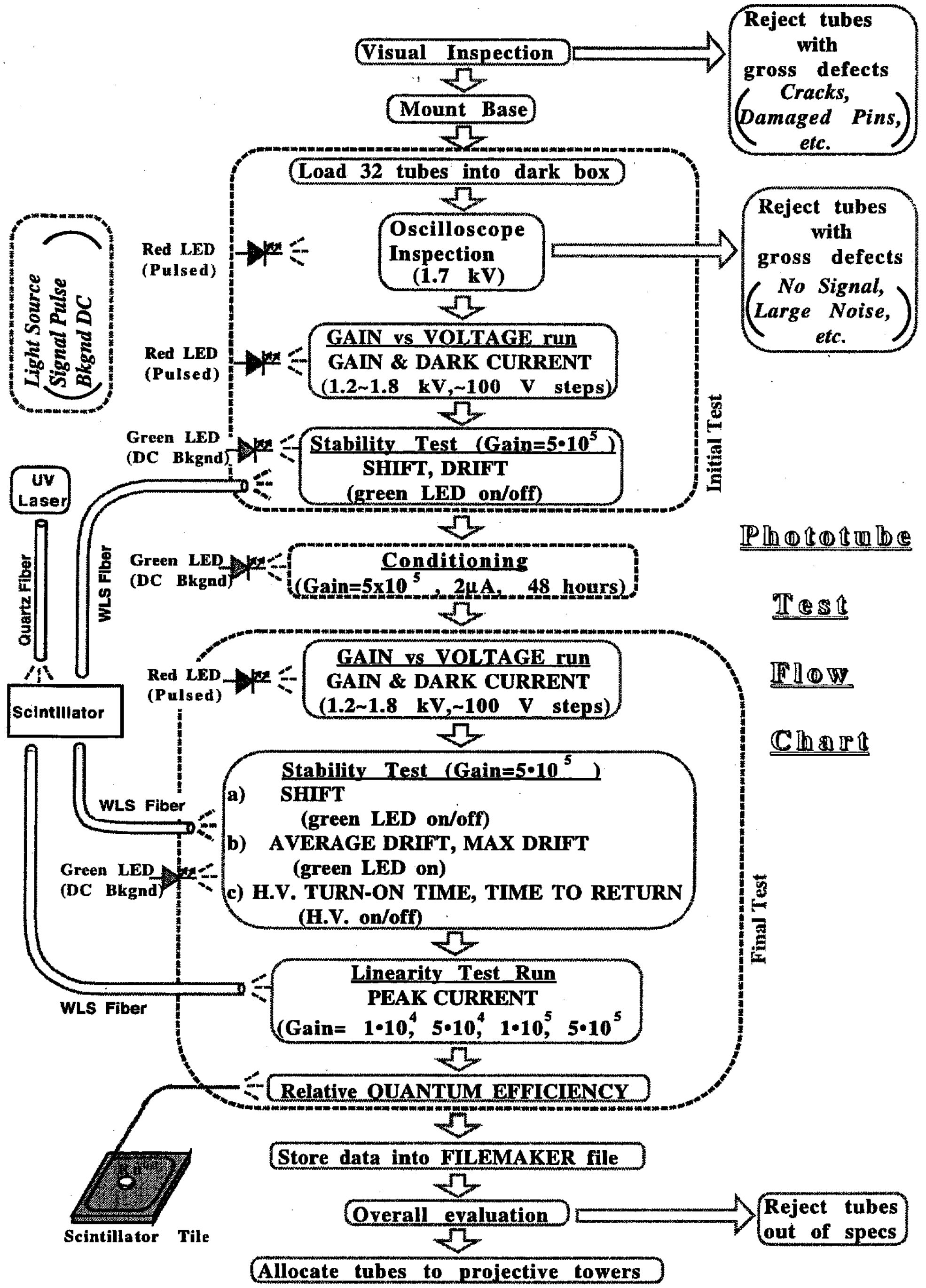

Fig. 7. Flow chart of the phototube test sequence.

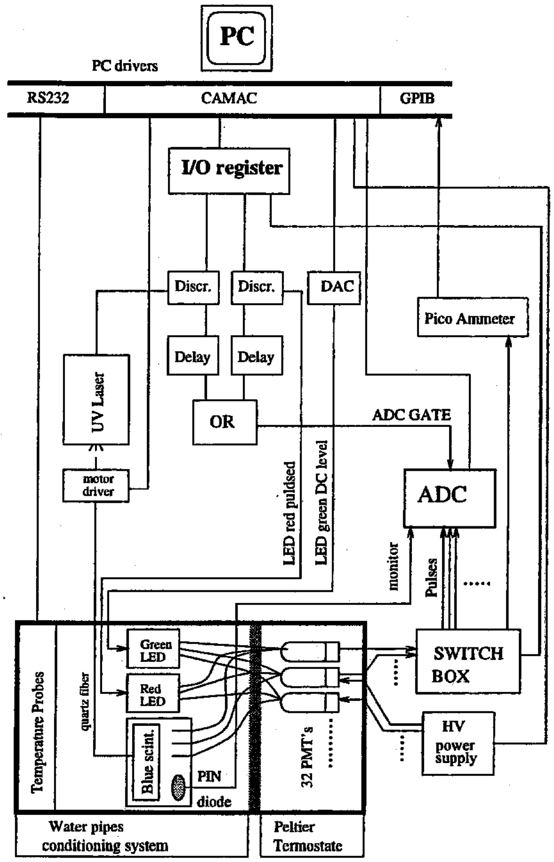

Fig. 8. Block diagram of the phototube test setup.

The atmosphere of the light-tight compartment was controlled to 23°±0.5° C by a Peltier unit with a thermocouple as a temperature sensor while the other side was water-cooled by pipes on the wall.

4.2.2. *Light sources: signal and background*

The role of the three types of light sources used in the test enclosure was to emulate the signal and the background light.

4.2.2.1. *Pulsed green light as the signal* The first was a pulsed green light that closely mimic the real light from the calorimeter. This was identical to the system implemented in the final Endplug calorimeter as a monitoring light source[16], described in Section 1.4.1.

Light from a nitrogen laser was brought to a block of blue plastic scintillator, Kuraray SCSN-38, via a quartz fiber. The scintillator block was set in a highly reflective cavity and 32 Kuraray Y-11 WLS fibers were inserted into the cavity in symmetrical positions with respect to the central axis of the scintillator block. After exiting from the cavity, the WLS fibers were spliced to clear polystyrene-core fibers, about 1 meter long each, for the optical connection to the tubes. The length of the portions of the WLS fibers inserted into the cavity, a few cm, were individually adjusted initially to equalize the light output to within 1 % at the far end of the clear fibers. Since the light from the nitrogen laser is a sharp narrow pulse, this combination of the scintillator, WLS, and clear fibers, emulated well the spectrum and the time structure of the real light pulse from the calorimeter.

The intensity of the UV light was controlled online. In the Fermilab system, a circular disk of linear-wedge neutral-density filter was used. In the Bologna system, a micrometric slide controlled the position of the quartz fiber with respect to the center of the light spot of the laser. The light output from the blue scintillator was monitored by a PIN diode which provided stable pulse-to-pulse normalization.

4.2.2.2. *Red LED's as the signal* The second was an array of 32 red (635 nm) LED's. These were used to measure the voltage dependence of the gain.

The red LED was used only to create photoelectrons and the color or the absolute light intensity was immaterial. It is because, as mentioned later (See Section 5.1.1), the gain was determined by the spread of the pulse height distribution relative to the pulse height. The red LED was plausible for such purpose because of its fast time response and stability.

4.2.2.3. *Green LED as the background* The third light source was an array of 32 green LED's (565 nm) to generate a DC current to mimic background current for measuring the stability of the tube response against background fluctuation.

The green light was to emulate the experimental condition in which the background current is real light from the calorimeter due to the multiple interactions from the same beam bunch crossing and also from the interactions from the preceding beam bunch crossings.

4.2.2.4. *Light source specifications, LED driver* The specifications of the nitrogen laser and the red and green LED's are given in Table 8.

Nitrogen Laser	
Model	Laser Photonics LN300 (Sealed N_2)
λ	337 nm
Power	250 μJ/pulse, 50 kW peak
Pulse width	5 nsec
Beam dimension	9 × 4 mm
Max rep rate	40 Hz
Red LED	
Model	Hewlett Packard HLMP 4101
λ_{peak}	635 nm
Green LED	
Model	Kingbright L53GT 30 mA, 30°
λ_{peak}	565 nm

Table 8
Light sources in test enclosure.

The circuit diagram of the 32-channel LED driver developed by INFN Bologna is shown in Fig. 9.

4.2.3. *Separate enclosure for relative Q.E. measurement*

A separate test enclosure was made solely to test relative quantum efficiency. The purpose was to track the consistency of the photocathode characteristics over the entire shipment of the tubes. 10 % of the tubes were sampled during delivery and subjected to this test. The box was made to house a single tube at a time. The measurement requires perfect stability of the light output at a wavelength matching the real light from the calorimeter. The number of photons needs to be relatively small so that the Poisson distribution can be well-defined to be able to determine the number of p.e's.

For this purpose, a package of tile-fiber was assembled using an identical combination of a scintillator tile and a WLS fiber spliced to a clear fiber as in the calorimeter[28]. The tile was a 10 cm square piece of 4-mm thick SCSN 38 and a string of Y-11 WLS fiber was looped twice in a groove engraved along the tile perimeter. At the exit from the groove, the WLS fiber was spliced to a clear polystyrene-core fiber which was strung to the front face of the sample tube. Specific care was taken to ensure a reproducible optical coupling to the sample phototube. The tile was illuminated by a Ru^{106} β-ray source and the trigger was generated by a pair of scintillation counters (2.5 cm square) sandwiching the tile. The number of p.e.'s was 2.5 on average. The pulse output from the phototube was measured by an ADC.

4.3. *Data acquisition system*

The test sequence for each of the test items was operated by a CAMAC system controlled by Fortran routines running on a MS-DOS PC at Fermilab or a Macintosh platform at Bologna.

The system trigger was provided via a CAMAC I/O register module, which generated a sequence of voltage levels and pulsed the laser or the red LED array for each test. A DAC and a motor control module combination was used to control the intensity of the laser-driven pulsed green light. The signal from the I/O register was also used to generate the ADC gate with the proper delay. Also the sequence of the DAC level to turn the green LED's on-off to mimic background current is controlled by this I/O register.

High voltage of the tubes were individually controlled by a multi-channel power supply.

Each of the anode outputs was branched into a pulse output via a serial capacitor and a DC output. The pulse outputs were connected to a multi-channel ADC unit in parallel and the DC outputs were fed one channel at a time to a common pico-ammeter via a multiplexer for cyclic measurement. A GPIB interface was used to read the pico-ammeter and also the temperature probe. The switch box was usually controlled by an I/O register whereas manual mode was useful for oscilloscope inspection of a selected tube.

For each test item, the sequence was automatic and the data were stored locally and later transferred to a DEC VAX Station for further analysis. All the data were compiled in a Macintosh File-

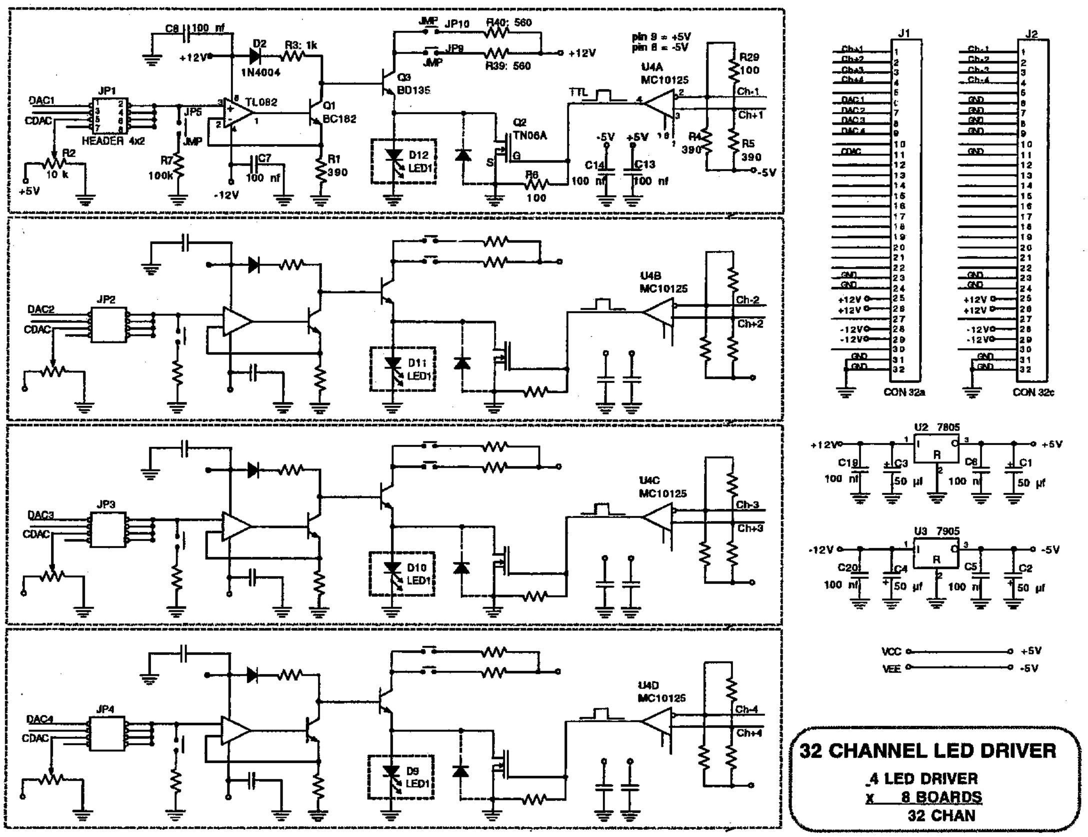

Fig. 9. Circuit diagram of the 32-channel LED driver.

MakerPro database and also posted on a dedicated website.

The specifications of the major components of the system are listed in Table 9.

High Voltage PS	LeCroy 1440 with two 1443 NF 2.5 kV, 2.5 mA, 16 chan
Pico-ammeter	Keithley 4685 Auto-ranging
ADC	CAEN C205 32 chan, charge integrating 15 bits dynamic range-full scale 112.5 pC 12 bits dynamic range-full scale 900 pC

Table 9
Equipment used in Bologna's data acquisition system.

5. Individual measurements and results

In this section, we describe the procedures and the results of individual measurements. For each item that was measured twice, we compared the two results, and we also compared our results with the data measured by the manufacturer.

5.1. *Gain measurement and voltage dependence*

5.1.1. *Method of relative gain measurement*

The method of the relative gain measurement is identical to what was employed by CDF before[29].

The gain is customarily defined as the gain of the electron multiplication process. In the presence of a non-negligible inefficiency in collecting the photoelectrons to the first dynode, the gain is defined as the ratio of the mean anode pulse height expressed in the number of electrons, μ_A, and the mean number of p.e.'s that reached the first dynode, $\mu_{p.e.}^{D1}$:

$$G = \frac{\mu_A}{\mu_{p.e.}^{D1}} , \tag{1}$$

where $\mu_{p.e.}^{D1}$ is a product of the mean number of p.e.'s emitted from the photocathode $\mu_{p.e.}$ and the electron collection efficiency of the first dynode ε_K^{D1}. Such "true gain" can be directly measured by establishing a single p.e. (SPE) peak in the anode pulse height distribution.

An indirect method is to utilize the spread of the anode pulse height distribution. In general the spread σ_A of the anode pulse height distribution is greater than the statistical fluctuation of the number of p.e.'s that reached the first dynode $N_{p.e.}^{D1}$ around the mean value $\mu_{p.e.}^{D1}$. It is because the electron multiplication fluctuates pulse-to-pulse due to the statistical fluctuation of the number of electrons through the processes of electron collection and the secondary electron emission of each dynode. Thus:

$$\sigma_A = f' \cdot G \cdot \sqrt{\mu_{p.e.}^{D1}} , \tag{2}$$

with

$$f' \geq 1 \tag{3}$$

and the gain G can be expressed by the measured quantities μ_A and σ_A as:

$$G = \frac{1}{f} \frac{{\sigma_A}^2}{\mu_A} , \tag{4}$$

where ${f'}^2$ was replaced by f for the sake of simplicity. However f is not calculable without detailed knowledge of the inter-stage electron collection efficiencies and the secondary emission ratios.

A simplistic approach for large scale measurement is to measure a relative gain

$$G' \equiv \frac{{\sigma_A}^2}{\mu_A} . \tag{5}$$

Thus G' is a factor f times G:

$$G' = f \cdot G . \tag{6}$$

As described in the next section, the relative gain in a wide range of voltage settings was determined by the mean pulse height relative to that of a single "anchor point" (See next section) times G', measured at the anchor poin using Eq. 5. Therefore, the relative gain of individual tube at any given voltage is normalized at the respective anchor point.

An advantage of this method is that it does not depend on the knowledge of the number of p.e.'s. For f to be valid as a relative measure of the gain, we assumed that f is common to all tubes in good approximation. This point is further discussed in Section 5.1.3.

Another method of measuring the gain is to take a ratio between the output current form the anode and the current flown into the photocathode (A/K ratio, hereafter) under illuminating DC light:

$$G_{A/K} \equiv \frac{I_A}{I_K} . \tag{7}$$

As mentioned in Section 3, this is the method employed by the manufacturer to measure the voltage for the nominal gain of 5×10^5 on each of the tubes. Since the current flown into the photocathode corresponds to the number of p.e.'s emitted from the photocathode, the ratio is equivalent to the ratio between μ_A and the mean of the number of emitted p.e.'s $\mu_{p.e.}$:

$$G_{A/K} = \frac{\mu_A}{\mu_{p.e.}} . \tag{8}$$

Using the following relationship:

$$\mu_{p.e.}^{D1} = \varepsilon_K^{D1} \cdot \mu_{p.e.} , \tag{9}$$

where ε_K^{D1} is the collection efficiency of the p.e.'s into the first dynode,

$$G_{A/K} = \varepsilon_K^{D1} \cdot G . \tag{10}$$

Therefore the ratio between G' and $G_{A/K}$ is:

$$\frac{G'}{G_{A/K}} = \frac{f}{\varepsilon_K^{D1}} . \tag{11}$$

Comparison between the data of G' and $G_{A/K}$ provided by the manufacturer will be made in the next section. Also a SPE peak gain measurement was performed on a small number of tubes by a Tsukuba University group and a KEK group. The manufacturer also made a measurement of the SPE gain together with A/K ratio on small ensembles of tubes. These are compared with the relative gain measurement in Section 5.1.4.

5.1.2. *Measurement of relative gain*

The gain of the tubes is only one element of a chain of multiple parameters that determine the calorimeter tower response. Therefore, the purpose of the gain measurement was not to determine the absolute value of the gain precisely but rather, in addition to testing the stability of the gain in time, to provide the initial setting for approximately uniform gain across $\eta - \phi$ span of the EM and HAD calorimeters, and finally to provide the voltage increment for adjusting the gain during the course of the run.

First, a scan was made by raising the voltage in $\sim 100\ V$ steps from 700 V up to 1800 V, and at each point, the pulse height distribution was measured for 10,000 flashes of red LED. Using the data, G' as defined by Eq. 5 was calculated and the first voltage setting, V_{anchor}, at which G' exceeded 1×10^6 was identified as an "anchor point". The gain at the anchor point, G'_{anchor}, ranged between 1×10^6 and $\sim 1.6 \times 10^6$ tube to tube[6].

Then only the value of G'_{anchor} was saved, and the relative gain of the rest of the voltage settings V were calculated by the mean pulse height $\mu_A(V)$ relative to that of the anchor point $\mu_A(V_{anchor})$ as:

$$G'(V) \equiv \frac{\mu_A(V)}{\mu_A(V_{anchor})} \cdot G'_{anchor} , \qquad (12)$$

with

$$G'_{anchor} \equiv \frac{[\sigma_A(V_{anchor})]^2}{\mu_A(V_{anchor})} . \qquad (13)$$

The measurement was made in the following sequence:

(1) set the high voltage,
(2) wait 10 min to stabilize,
(3) measure the dark current,
(4) flash red LED 10^4 times for which the output was recorded.

Data taking was divided into two sequences at fixed light levels. The higher light level sequence (with about 4000 photoelectrons) scanned from 700 V to 1200 V, while the second (with about 300 photoelectrons) scanned from 1000 V to 1800 V, in $\sim 100\ V$ steps. These voltage settings corresponded to the range of the relative gain between 10^3 and 10^7, depending on the tube. Then the two sets of data were merged by normalizing at three successive overlapping voltage settings to make a log-log plot of G' vs. V. The plot was then fitted with a straight line with a formula:

$$\log_{10} G' = K + P \cdot \log_{10} V , \qquad (14)$$

which is a power law dependence of the relative gain on the high voltage:

$$G' = 10^K \cdot V^P . \qquad (15)$$

The fit was constrained to pass through the anchor point. Using the fitted parameters K and P in the above equation, the voltage for any value of the relative gain would be calculated.

This formula resulted in excellent fits for all tubes.

Figs. 10 (a) and (b) are the histograms of these two parameters in which the results of the initial and final tests are overlaid.

The above figures show a consistent shift towards a greater (smaller) value of K (P) of the final test result with respect to the initial test result. Such overall shift is also visible in the scatter plots between the initial and the final test results, shown in Figs 11 and 12, the tube-by-tube. The 45° lines are drawn to guide eyes. Despite such shift in the individual parameters, the strong correlation between the two parameters shown in Fig. 13 essentially cancels out the effect and the resultant relative gain is in good agreement between the two measurements. In this figure, the data sets of the initial and the final tests are overlaid showing a similar pattern between the two data sets.

Fig. 14 is a scatter plot of the voltage for the relative gain of 5×10^5 between the initial test data and the final test data. The voltages were calculated using the parameterization of Eq. 15. The 45° line that corresponds to the case of exact match is to guide the eyes.

It should be noted that this relative gain vs. voltage measurement was made twice, first at the beginning of the initial test sequence and then at the beginning of the final test sequence. Therefore the two measurements were separated by an average

---

[6] G'_{anchor} spread up to 2×10^6 for about 350 tubes due to a temporary change of the procedure.

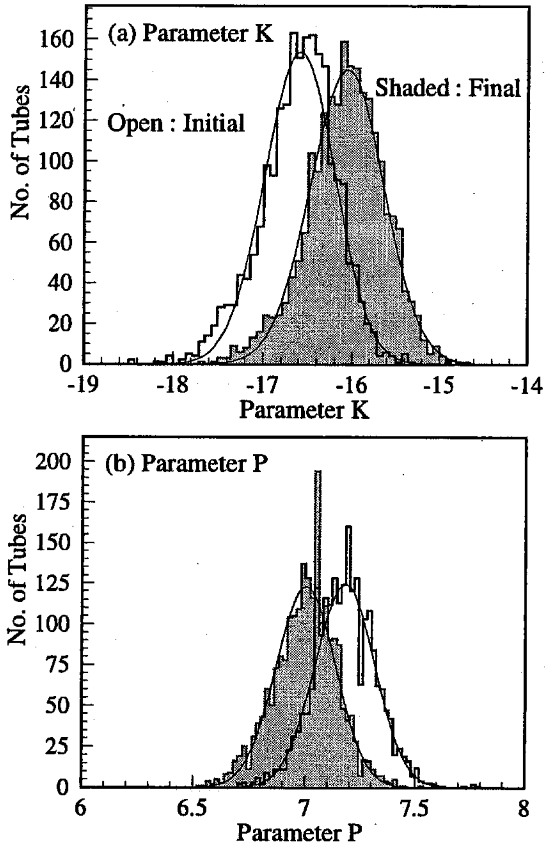

Fig. 10. Distribution of the power law parameters (a) K and (b) P. The initial (open) and the final test data (shaded) are shown together. Curves are Gaussian fit.

of 15 months, half a year minimum and 3.5 years maximum.

Overlaid in the same figure is a scatter plot between the manufacturer's data of the voltage for the nominal gain, i.e. $G_{A/K}$, of 5×10^5 shown previously in Fig. 5 and the final test data.

If the manufacturer's data were normalized by a factor of 0.92, the average of the tube-by-tube ratios between the two measurements, the two scatter plots overlap quite well. The agreement of the manufacturer's data with our data with such normalization is clearly observable in the histograms in Fig. 15. Histograms of all three data sets are overlaid in this graph.

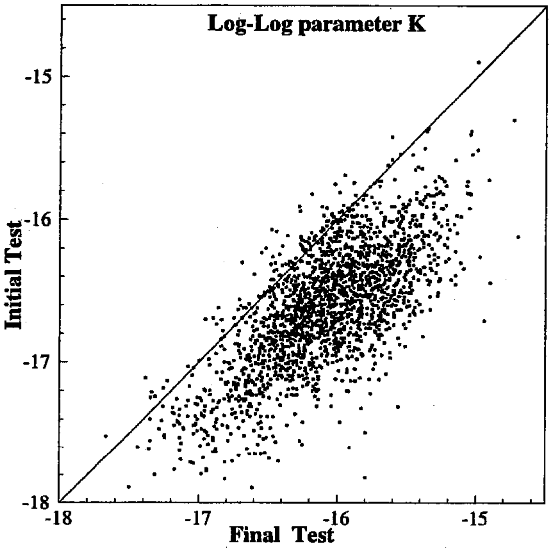

Fig. 11. Scatter plot between the initial and the final test data of the parameter K. A diagonal line corresponding to exact equality between the two sets of data was drawn to guide eyes.

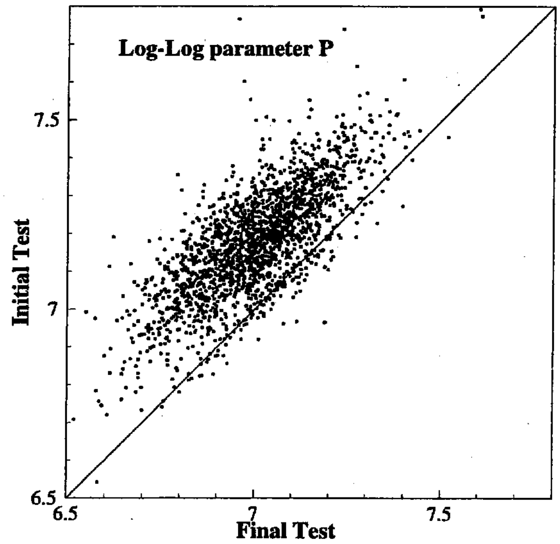

Fig. 12. Scatter plot between the initial and the final test data of the parameter P. As in the previous figure, the diagonal line corresponds to exact equality between two data.

The agreement between these three measurements is further examined in Fig. 16, in which the distribution of the tube-by-tube difference between the final test result and the initial test result, and

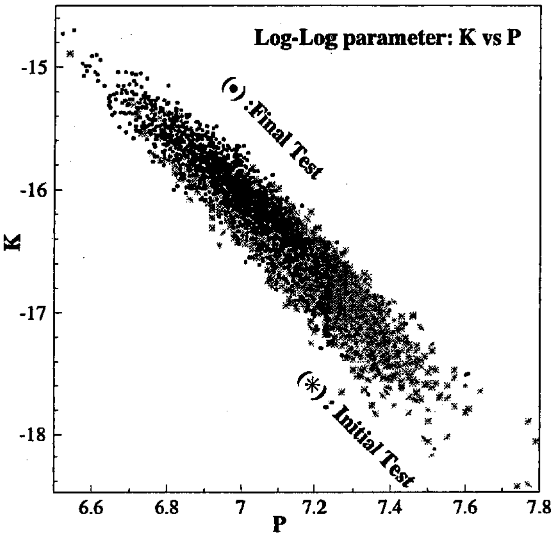

Fig. 13. Scatter plot of log-log plot parameters, K vs. P. The data sets of the initial and the final tests are overlaid.

also the difference between the final test result and the normalized manufacturer's data are plotted. The mean value is close to zero and the R.M.S. of the distribution is less than 3 %.

If we multiply the voltages for the relative gain of 5×10^5 by a factor of 1/0.92 to normalize to the manufacturer's voltage distribution for $G_{A/K} = 5\times10^5$, the corresponding relative gains are calculated to have a mean of 8.9×10^5 ($\sigma = 1.2\%$), a factor of 1.79 ± 0.02 times the original relative gain. We discuss what the relationship between the gains of various definitions are expected to be in the next section.

5.1.3. *Discussion on relative gain measurement*

The relative gain G' defined in Eq. 5 is equal to the true gain G defined by Eq. 4 if the spread of the anode pulse height distribution is solely from the statistical fluctuation of the number of p.e.'s collected into the first dynode $N^{D1}_{p.e.}$. However, there are additional statistical fluctuations due to non-unity electron collection efficiency and the secondary electron emission process on each stage, especially on the first few dynodes.

As of this writing, we retrospectively examined what actually f , the ratio between G' and G as defined in Eq. 4, was, prompted by a comment by

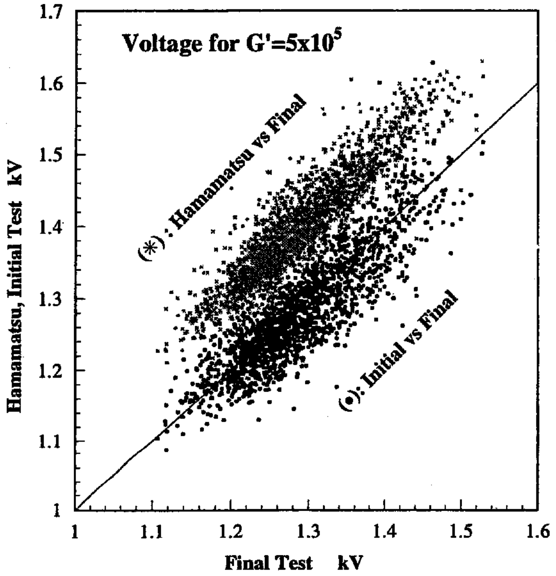

Fig. 14. Scatter plot of the voltage for the nominal gain of 5×10^5. The initial test data vs. the final test data is overlaid with the manufacturer's vs. the final test data. The nominal gain is the relative gain G' for the initial and the final test data and A/K ratio $G_{A/K}$ for the manufacturer's data.

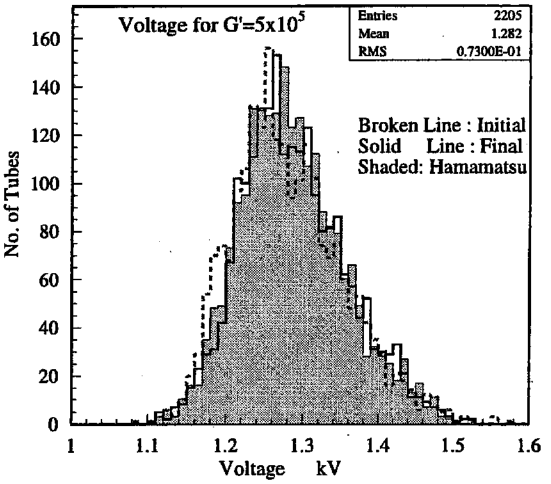

Fig. 15. Histograms of the voltage for the nominal gain of 5×10^5. The histograms of the data of the initial test (broken line) and the final test (solid line) are overlaid with the manufacturer's data (shaded). The definition of the nominal gain is the same as in the previous figure. The voltage of the manufacturer's data was normalized by a factor 0f 0.92.

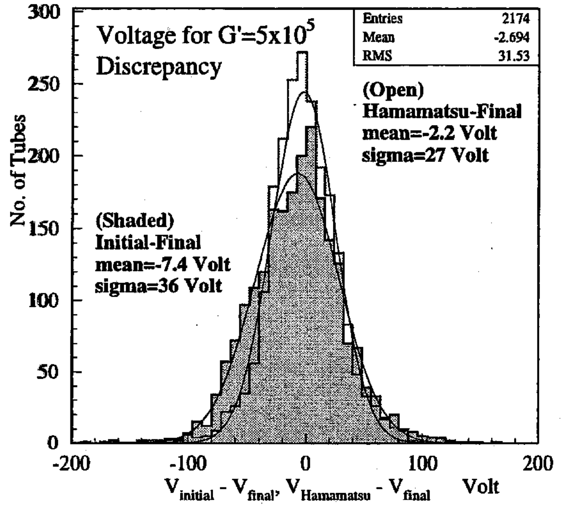

Fig. 16. Histograms of the difference of the voltage for the nominal gain of 5×10^5 among three measurements. The difference between the final test and the initial test, and also between the final test and Hamamatsu's measurement are overlaid. As in the previous figure, Hamamatsu's data are normalized by a factor 0.92. Definition of the gain for each of the three data sets is the same as the previous two figures.

one of the referees of this article.

We conclude that the following is the correct expression of f[27,30,31]:

$$f = 1 + \frac{1}{\Delta_1} + \frac{1}{\Delta_1\Delta_2} + \ldots + \frac{1}{\Delta_1\Delta_2\cdots\Delta_{10}}\,. \tag{16}$$

where Δ_i is the effective i-th dynode incremental gain which is a product of the secondary electron emission ratio and the electron collection efficiency to the next dynode. (See APPENDIX for detail.)

The relative gain we measured was supposed to be greater than the true gain by this factor.

Since the contribution of the terms diminish successively, f is mainly determined by the first few terms. Based on available data on the phototube, we estimated the value of f to be ~1.2 depending on the dynode material, especially one for the first dynode[26,27].

We can also estimate the ratio between the relative gain and $G_{A/K}$. The ratio in Eq. 11 is expected to be 1.3 ~ 1.5, taking 80 ~ 90%[27] as the value of ε_K^{D1} [7]. This value is significantly smaller than the observed factor ~1.8 mentioned in the previous section.

5.1.4. *Supplemental gain measurement*

Supplemental data that augment the discussion in the previous section were supplied by two groups, a Tsukuba University group[32] and Hamamatsu Photonics[33].

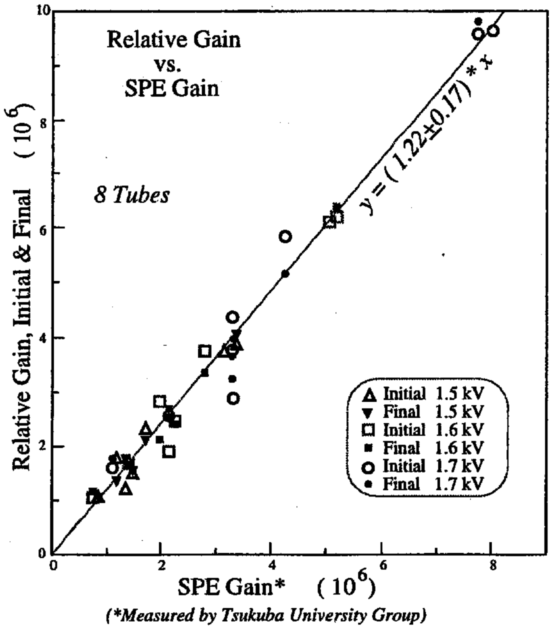

Fig. 17. Scatter plot of the relative gain G' vs. the true gain G measured by observing SPE peak. The straight line was fit to 43 usable points through origin.

The Tsukuba University group measured SPE peaks on eight tubes randomly selected from our reserve of R4125's. It is a direct measurement of the true gain G of electron multiplicity. The measurement was made at 1.5, 1.6, and 1.7 kV and the result is compared with the relative gain G' in the scatter plot shown in Fig. 17. A linear fit through the origin yielded a slope of 1.22 ± 0.17, in good agreement with the expected value of the ratio f estimated in the previous section.

---

[7] The cathode-first dynode voltage is ~140 ~ 190 V for the anchor point voltage of ~1.3 ~ 1.7kV.

An additional set of data was measured by Hamamatsu Photonics for ten tubes. Out of which, three were out of the eight tubes the Tsukuba University group used for the above mentioned measurement. The rest, seven tubes, were from Hamamatsu's own reserve of R4125's. Two types of voltage divider configurations were used:

F-type : 2 : 1 : ... : 1 : 2 : 4 : 3
T-type : 1.5 : 1 : ... : 1 : 1.2 : 1.8 : 3.6 : 3.3
(F-type is identical to CDF's divider.)
and all measurements were made at 1.5 kV. The A/K ratio's were measured on all ten tubes and the SPE gain's were measured on nine tubes. Data of the A/K ratio measured in '94, '97, and '98 with T-type divider and the SPE gain measured by a KEK group were provided for subsets of small number of tubes, with some overlapping among them.

These results are plotted in Figs. 18, 19, and 20.

Though limited in statistics, one can see in Fig. 18 that the SPE gain measured by the Tsukuba University group and the KEK group agree with the data measured by Hamamatsu within 4 %.

A proportionality between the A/K ratio and

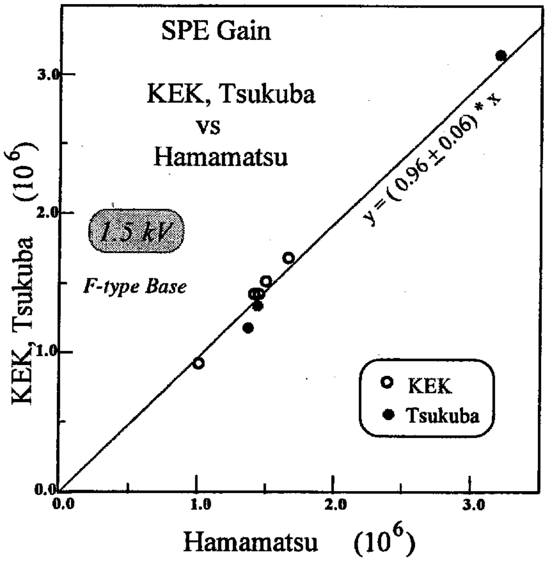

Fig. 18. Scatter plot of SPE gain: data measured by a Tsukuba University group and a KEK group vs. data measured by Hamamatsu.

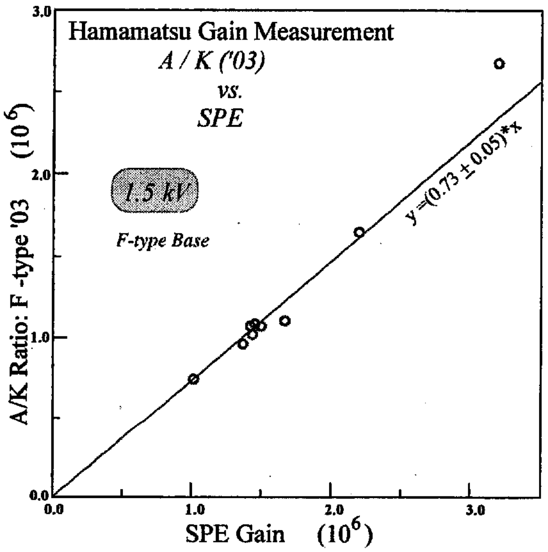

Fig. 19. Scatter plot of A/K current ratio vs. SPE gain measured by Hamamatsu.

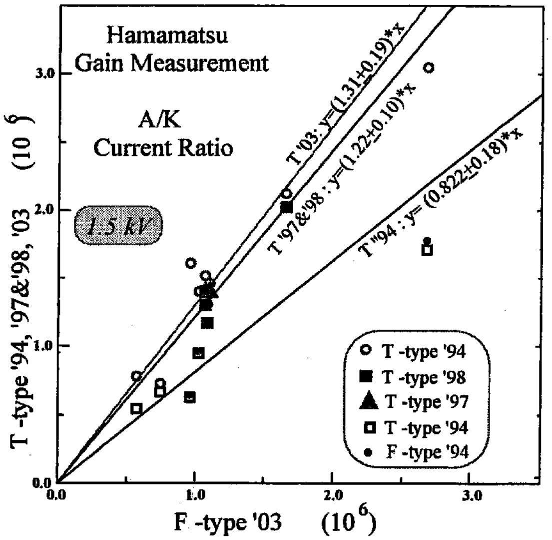

F-type base : 2 : 1 : .... : 1 : 2 : 4 : 3
T-type base : 1.5 : 1 : ... : 1 : 1.2 : 1.8 : 3.6 : 3.3

Fig. 20. Scatter plot of A/K current ratios measured in '94, '97, '98, '03 using T-type divider vs. A/K ratio measured in '03 using F-type divider.

the SPE gain is clearly seen in Fig. 19.

The tubes Tsukuba University measured were from our spares which had the original data of A/K ratio dated '94 through '95 provided by Hamamatsu. In Fig. 20, the three points marked as F-type '94 are derived from such original A/K ratio. For these, the original A/K ratio of 5×10^5 was scaled to 1.5 kV using the parameter P of the relative gain parameterization (Eq. 15 in Section 5.1.2).

In this figure, one notices that there are 20 to 30 % discrepancies between the A/K ratios measured at different times.

From the above, a general observations are:

a) the SPE gain measurement is reproducible and therefore the most reliable method for measuring the gain.

b) In contrast, the A/K current ratio measurement seems to suffer from 20 to 30% normalization error [8].

Using the above set of data, we can derive the ratio between the relative gain G' and A/K ratio i.e. $G_{A/K}$ (Eq. 7 in Section 5.1.1) as

$$\frac{G'}{G_{A/K}} = \frac{G'}{G_{SPE}} \cdot \frac{G_{SPE}}{G_{A/K}} . \qquad (17)$$

To calculate the above, we use

$$\frac{G'}{G_{SPE}} = 1.22 \pm 0.17 \qquad (18)$$

measured by eight tubes as shown in Fig. 17, and

$$\frac{G_{SPE}}{G_{A/K}} = 1.61 \pm 0.22 , \qquad (19)$$

taking a ratio between '94 data of A/K ratios, with T-type (4 points) and F-type (3 points) combined, and the corresponding SPE gains combining the Tsukuba data and the KEK data. The result is:

$$\frac{G'}{G_{A/K}} = 1.96 \pm 0.38 . \qquad (20)$$

This value is consistent with the observed value of $G'/G_{A/K} \sim 1.8$ as mentioned in the previous section.

5.1.5. *Summary on gain measurements*

Though the statistical significance is limited, the supplemental measurement on the SPE gain, which seems to be a reliable measurement, provided us an evidence that the relative gain G' we measured is consistent with the value expected from the true gain G with the factor f in between.

The discrepancy between the observed ratio between G' and $G_{A/K}$ and the expected value is most likely due to the normalization error in the A/K ratio measurement.

Despite such a discrepancy, there is obviously a good correlation between our data and the manufacturer's data as exhibited in Figs. 14, 15, and 16. This indicates that both of the data sets, our relative gain data and the manufacturer's data, are self-consistent within respective data set. Which, together with the good proportionality between the relative gain and the SPE gain observed in Fig. 17, further indicates that the factor f is common to all tubes in good approximation. This may be explained by the fact that f is primarily a function of Δ_1 which is more or less on a saturated plateau as a function of the voltage. On the other hand the gain is a product of the inter-stage gains of all dynodes and minor variations of the values of the parameters of individual dynodes multiply and therefore the gain, and conversely the voltage for a certain gain, can vary significantly tube to tube.

The tight correlation between the three measurements, the initial test, the final test, and the manufacturer's measurement, is not only a demonstration of the relevance of the procedure, but also, considering the time elapsed between the three measurements, an assurance that the gain is stable over time and can be traced closely by adjusting the voltage using the measured parameters.

Since the energy resolution of EM needs to be more stringent than HAD, further tuning of the relative gain uniformity was made before the the run by measuring cosmic ray muons tower by tower[10]. The absolute response of the calorimeter against incident particles will be determined *in situ* because most of the Endplug calorimeter ($\eta \lessapprox 2$) is fully covered by the tracking system that provides an absolute momentum measurement. It will be aided by the absolute calibration using copious

---

[8] In our understanding, the cathode and the anode currents are separately measured to calculate the A/K ratio. We suspect such a process is prone to an overall error in normalizing the data for the different incident light intensity.

electrons from $Z^0 \to e^+e^-$ decays with one electron being measured in the central region of the CDF detector[23], where an *in situ* absolute energy calibration is made by the central tracking system in a magnetic field.

Measuring the gain of phototubes for visible range photons is not a simple matter for many reasons. Though the SPE gain and A/K current ratio are both well defined and can be measured in good accuracy, it is not directly applicable to calculate the gain for the incident photons. Therefore the choice of the method of the gain measurement has to be made depending on the practicality for one's needs.

5.2. *Dark current*

The dark current was measured twice, once in the initial test and a second time in the final test. Dark current was measured at each voltage step of the gain-voltage relationship measurement from 700 V up to 1800 V as described in Section 5.1.2. However the record was kept only for the measurement taken at the anchor point which ranged between 1×10^6 and 1.6×10^6 in the gain. Therefore a proper normalization needs to be made in order to compare the two sets of data and the data provided by the manufacturer which was measured at the nominal gain of 5×10^5.

Plots of the dark current in logarithmic scale against the voltage for 28 arbitrarily chosen tubes consistently show that they were well fitted by straight lines from which only the data points above ~1700 V slightly deviated [9]. The functional form of the fit was, therefore:

$$I_{dark} = exp(aV + b) \ . \qquad (21)$$

Based on this observation, we plotted the dark current against the voltage in Fig. 21 for all, ~2200, tubes with the dark current in log scale.

The dependence of the dark current on the voltage setting is observable in this plot. To see it more clearly, we plotted the centroid of each cluster in Fig. 22.

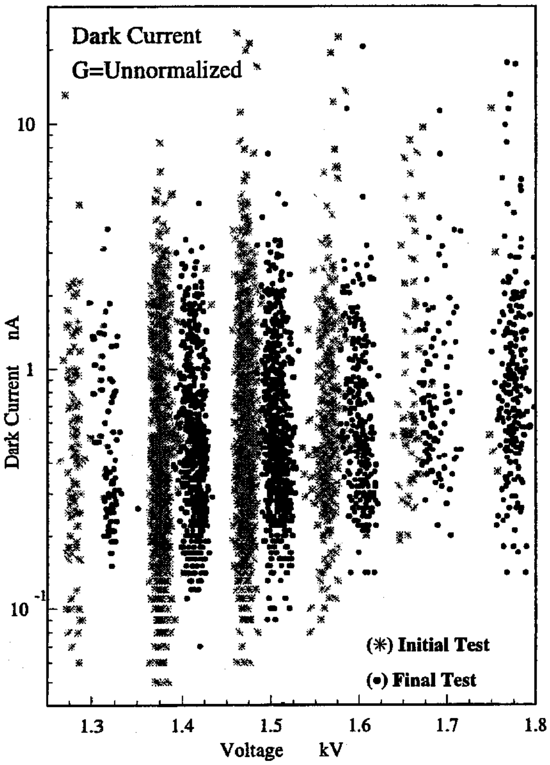

Fig. 21. Scatter plot of the dark current vs. the voltage with the vertical axis with logarithmic scale. In order to make the initial and the final test results discernible, the points for the initial (final) test were horizontally offset by -15 V (+15 V) from the true voltage values.

The two data sets, the initial and the final tests, are similar and a straight line gave a plausible fit. The χ^2-fit to the two data sets combined resulted in:

$$a = 1.31 \pm 0.17 \text{ and } b = -2.25 \pm 0.25 \ , \qquad (22)$$

as drawn in the plot [10].

By this parameterization, a measured dark current can be scaled to a different voltages as:

---

[9] Similar behavior was observed for phototubes from other manufacturers[34].

[10]. These values are in agreement with the fit to the individual tubes mentioned above. The avarages of the parameters from the fit to the data of 28 tubes were

$$a = 1.29 \pm 0.42 \text{ and } b = -2.89 \pm 0.27 \qquad (V in\ kV). \qquad (23)$$

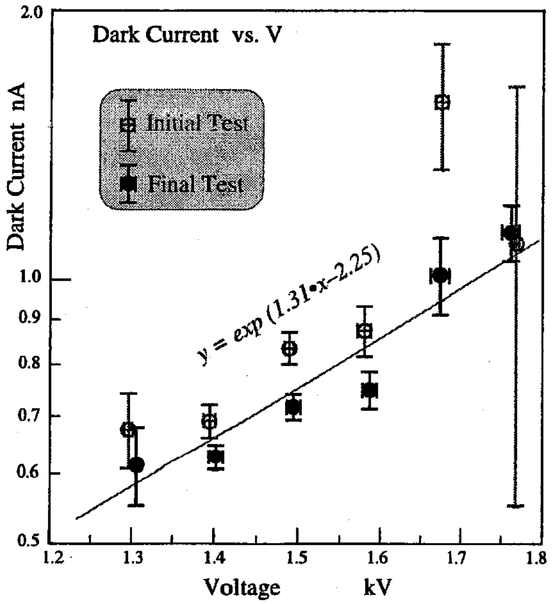

Fig. 22. Scatter plot of the centroids of the clusters in the previous figure. The straight line is a fit to the combined twelve points.

$$I_{dark}(V) = I_{dark}(V_{meas}) \cdot exp[a(V - V_{meas})] \,. \tag{24}$$

After normalizing the three data sets for the nominal gain of 5×10^5 using the above formula, they are compared in the histograms in Fig. 23 and also in Fig. 24, scatter plots of the manufacturer's data and the initial test data vs. the final test data.

In these plots, the data measured at the anchor points were scaled to the voltages that corresponded to the manufacturer's nominal gain of 5×10^5, i.e., 1/0.92 times the voltage for the relative gain of 5×10^5 [11].

In Fig. 23, one can observe that the population under the peak did not change between the manufacturer's measurement and our measurement but the peak was enhanced by the shrinkage of the components in the tail of higher values in the manufacturer's data. This may indicate that the dark current becomes quieter in time. Though there was a conditioning process between the initial test and the final test, the difference between the two dark current data is insignificant.

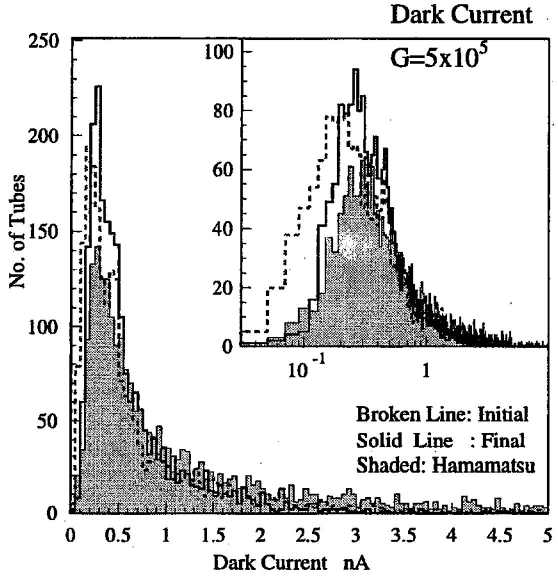

Fig. 23. Histograms of the three sets of data, Hamamatsu's, initial, and final test data, are overlaid. A normalization was made by voltage-scaling (Eq. 24) to Hamamatsu's data for the nominal gain of 5×10^5. Superimposed is a semi-log plot of the same histogram. The voltage for the nominal gain of 5×10^5 was taken as the voltage for the relative gain of 5×10^5 times 1/0.92.

Final selection was made requiring that the dark current at the relative gain of 5×10^5 be less than 5 nA using the final test data. Ten tubes were rejected based on this criterion.

5.3. *Linear dynamic range*

"Peak current" was defined as the peak point of the output current pulse shape when illuminated by laser-driven pulsed green light. Based on the pulse shapes observed on a number of samples, we took a simplistic assumption that the pulse shape was triangular with a base of 14 ns and converted the measured charge into the peak current. This pulse shape mostly reflects the decay time of the Y-11 fluor of the WLS fiber, although the actual pulse shape has an exponential tail beyond 14 ns. Therefore, the peak current thus deduced from the measured charge is a slight overestimate of the ac-

---

[11] We also considered a normalization by the ratio of the gains. The result was peaking at much lower values compared to Fig. 23.

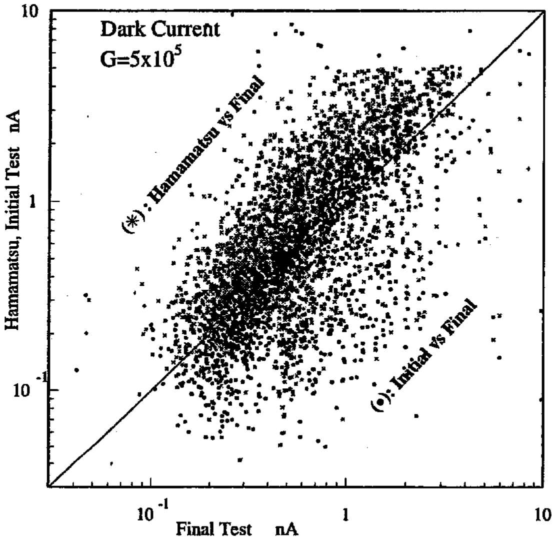

Fig. 24. Tube by tube scatter plot of the dark current at the nominal gain of 5×10^5, The Hamamatsu's data and the initial test data vs. the final test data are overlaid. The same normalization to the Hamamatsu's data as the previous figure was applied.

tual peak of the signal pulses.

As mentioned in Section 4.2.2.1, the input light intensity was varied by changing the intensity of the UV laser light that illuminated the scintillator-WLS fiber assembly. The monitoring PIN diode was separately tested for its linearity. Though there is a minor non-linearity at the small signal end, it is linear well over the range of the light intensity relevant to this measurement.

The measurement was made at four different relative gain values, 1×10^4, 5×10^4, 1×10^5, and 5×10^5. The general trend was that the peak current would rise linearly up to a certain point and then start a downward deviation with exception of a small number of tubes that exhibited upward deviation before rapid downfall.

The procedure for determining the maximum peak current is illustrated in Fig. 25, using a fake data set.

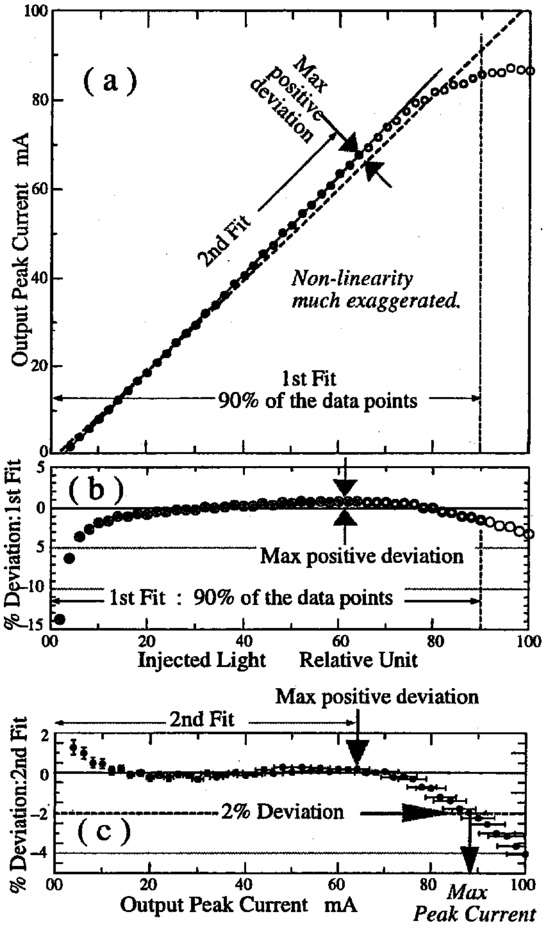

Fig. 25. Cartoon illustrating the procedure to determine the maximum peak current(See main text)

In *a* of the above figure [12], the output peak current is plotted against the injected light intensity. On this plot we make two steps of linear fit. The first fit (lower, broken line) is made to the portion of the lower 90 % of the entire range. The deviation from the fitted line is plotted against the output peak current in *b*. The point of the maximum positive deviation is determined, as shown by arrows, and then the data up to this point in *a* is re-fitted by another straight line (upper, solid line). The deviation from the second fit is plotted in *c*. The peak current at the point which deviated from the fitted line downward by 2 % or greater is defined as the maximum peak current.

---

[12] While the data set for *b* and *c* is reasonably resembling the trend of real data, the data set for *a* is made by adding 5 times *b* to a linear term in order to make the nonlinearity visible.

It should be noted that the non-linearity at lower end of the plots is due to the non-linearity of the PIN diode, but not the phototube characteristics. For most of the tubes the decrease of the response beyond 2 % deviation point is gradual. For example, the point of deviation by 5 % is more than 10 % greater in the injected light intensity than 2 % deviation point.

Due to limitation of the system, the injected light intensity was not enough to reach the 2 % deviation point on some of the tubes. For those tubes, the maximum of the peak current reached was recorded as "light-limited maximum". These values, therefore, represent the lower limit of the maximum peak current.

In Fig. 26, the distributions of the maximum peak current for the relative gain of (a) 1×10^4, (b) 5×10^4, (c) 1×10^5, and (d) 5×10^5, are plotted, respectively.

The shaded histograms are the maximum peak current at the 2 % deviation point as defined above and the open histograms are the light-limited maximum current. The number of the data entries of the light-limited maximum current is greater for smaller gains. The ranges of the two histograms for each gain value are quiet similar.

Fig. 27 is a tube-by-tube scatter plot of the maximum peak current vs. the voltage. The data for the relative gains of 1×10^4, 5×10^4, 1×10^5, and 5×10^5 are plotted in different symbols. The measured currents for two different definitions of the maximum peak current are plotted together.

An enlarged plot for the lowest gain, 1×10^4, shows that the distributions of the light-limited maximum current and the true peak current are quite similar.

The general observation on Fig. 27 is that the maximum peak current increases almost linearly with the voltage.

Most of the tubes were well above the minimum value originally specified and only a small number of tubes were below the specification for one or more of the above four gain values.

In the final selection, only the criteria for the actual operating values of the relative gain, 2.5×10^4 for the EM and 2.5×10^5 for the HAD, were considered. Tubes were not required to satisfy both of the criteria and those that passed either of these

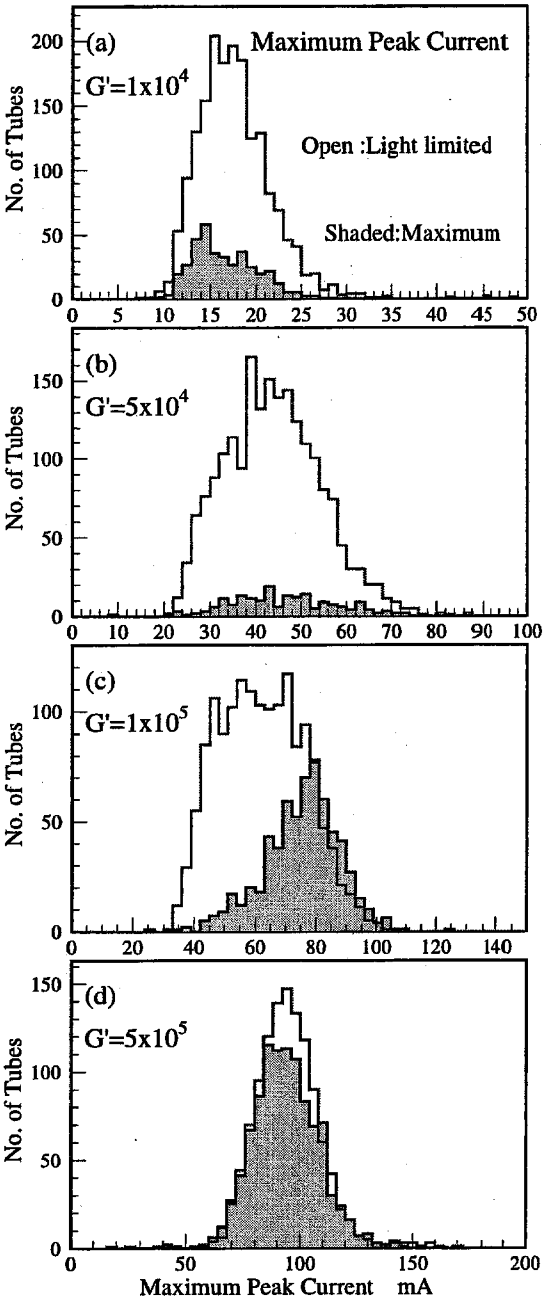

Fig. 26. Distribution of the maximum peak current for the relative gain G' of (a) 1×10^4. (b) 5×10^4. (c) 1×10^5. and (d) 5×10^5. The true maximum peak current (shaded) and the light-limited maximum current(open) are overlaid.

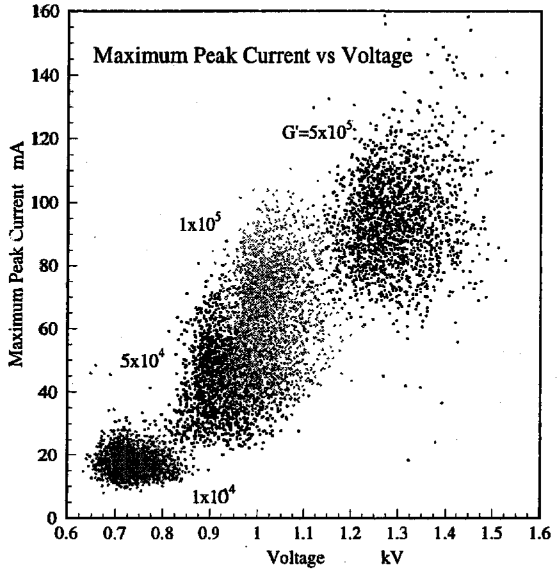

Fig. 27. Scatterplot of the maximum peak current against the voltage at the relative gain of 1×10^4, 5×10^4, 1×10^5, and 5×10^5.

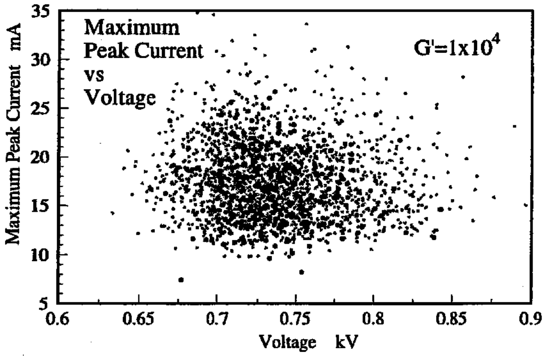

Fig. 28. Scatterplot of the maximum peak current for the relative gain of 1×10^4. Maximum peak current : larger dots. Light-limited maximum : smaller dots.

criteria were allocated to the EM or the HAD towers accordingly. Consequently no tube was rejected based solely on this quantity.

Then the tubes were sorted based on the maximum peak current for a relative gain of 2.5×10^4 (2.5×10^5) for EM (HAD) and assigned to the towers in the order of η. The tubes of higher peak current were assigned to the higher η towers.

The exceptions are the two highest η towers, the one that subtends η =2.6 ~ 3.0 and the othe that subtends η =3.0 ~ 3.5, which have poor shower containment due to small physical dimension in azimuthal direction, especially for hadronic shower. Also, it was recognized that those towers would not be used to measure single particle energy since the limited coverage of the inner tracking system, composed of Central Outer Tracker, Silicon Vertex Tracker, and Intermediate Silicon Layers[3], would lead to poor pointing accuracy. Therefore, those towers were not required to be allocated with tubes of high maximum peak current.

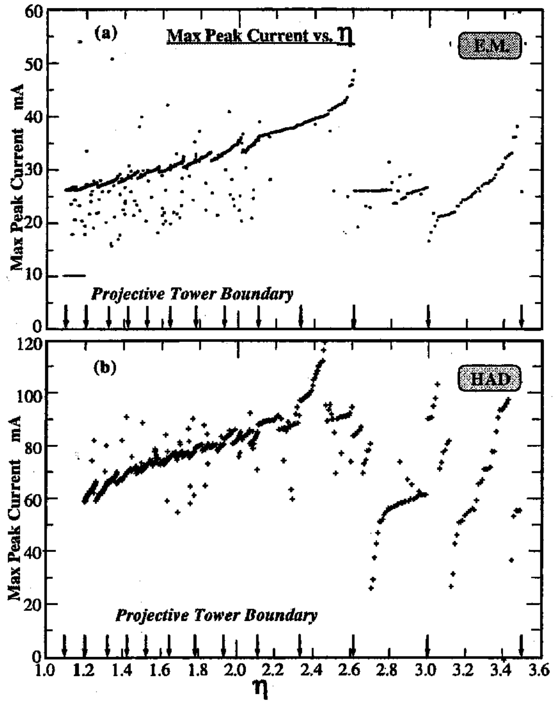

Fig. 29. Maximum peak current of the tubes against the η of the allocated projective towers of (a) EM and (b) HAD.

Figs. 29 (a) and (b) are the plots of the maximum peak current against the η of the assigned EM and HAD towers, respectively.

In these figures, the points in each η-bins, marked by vertical arrows on η-axis, represent the projective towers of different ϕ-bins with the order in ϕ being converted into the sequence along η-axis. Thus, there are 48 (24) points in each of the η-bins between 1.1 and 2.11 (between 2.11 and

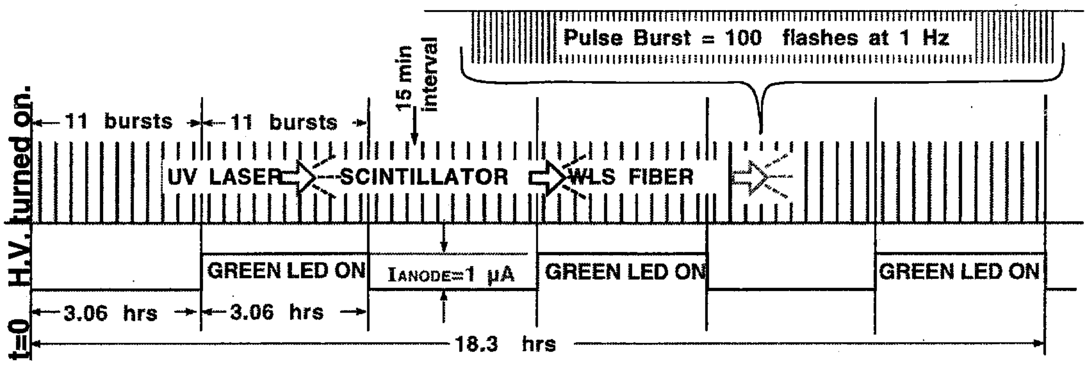

Fig. 30. Light flash sequence for stability test.

3.48).

5.4. *Stability*

The phototubes are the only active elements in the chain that convert the energy deposit in the calorimeter into an electrical signal. The others are passive components and a change in time, if any, in the response or the transmission characteristics, is expected to be gradual and small. Therefore the stability of the phototubes for both short and long term is essential for the accuracy of the calorimetric measurement.

In the short term, the phototube gain must be stable within the specified limit against changes in the accelerator luminosity which cause fluctuations in the light input from background events. Long term stability is required within the time interval of calibration, either by laser pulsing or by much less frequent radioactive source scanning. The laser pulsing is expected to be made in the pauses between beam stores, which takes place in about a half day cycle initially and possibly longer when the luminosity leveling scheme is implemented.

5.4.1. *Shift of the gain due to background fluctuation*

In actual runs, the inter-stage voltage is affected by the energy flow into each tower which is averaged over many beam bunch crossings due to the large time constant of the resistor chain of the bases. Therefore the effect of fluctuations of the background signals needed to be studied.

In this test, the signal was the laser-driven pulsed green light. The background current was induced by the green LED.

A cartoon in Fig. 30 shows the sequence of the pulsed signal and the steps of DC background light.

Starting from t=0 at which the high voltage was turned on to give a relative gain of 5×10^5, the laser was flashed 100 times at a rate of 1 Hz in a burst at 15 minute intervals. The response of the tubes to each flash was recorded. The first 11 bursts were with the green LED off and the next 11 bursts were with the green LED on to draw an anode current of $1\mu A$ on each tube, the maximum background current expected in Run II.

This cycle of LED off and on was repeated three

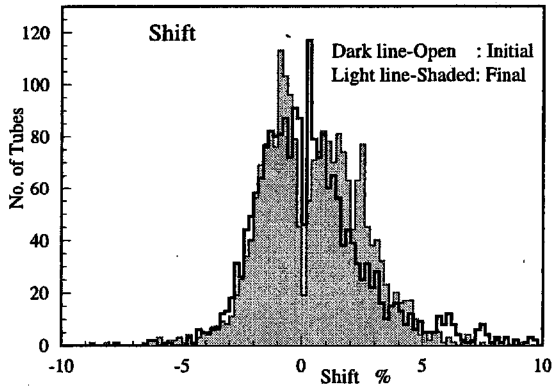

Fig. 31. Distribution of Shift. The definition of the quantity is given in the main text. The initial and the final test results are overlaid.

times, taking about 18 hours in total. In each of the pulse bursts, the response to each of 100 flashes was averaged as the response to the burst. Then three such responses were averaged for LED off and on, respectively, and the difference was defined as "Shift".

Fig. 31 is the histograms of this Shift measured in the initial test and the final test. About half of the tubes showed an average positive Shift of 1.9% in the gain and the remaining half showed a negative Shift of 1.3% on average.

The good agreement between the initial and the final test data indicates that the 'conditioning' inserted between two tests did not affect this quantity. The consistency between the initial and the final tests is also shown in Fig. 32.

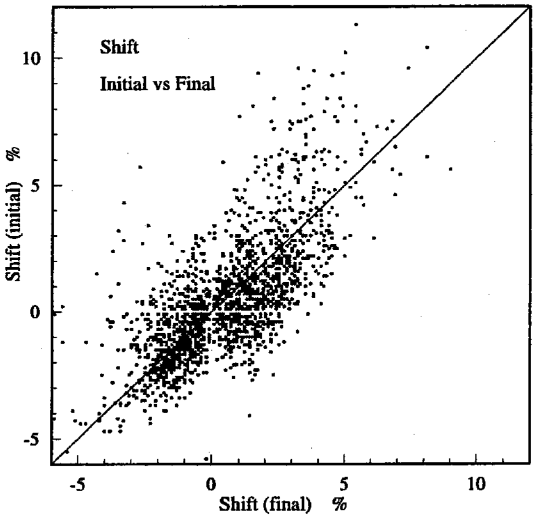

Fig. 32. Scatter plot of "shift" between the initial and the final test.

Based on the final test result, 49 tubes exceeded the specified limit of ±5 % and were rejected. It should be pointed out that though the Shift is a measure of a direct change of the gain, the condition to measure the Shift, 1 μA change in the background current, does not occur instantaneously in the actual experiment. Because of the long time constant of the base circuitry, a large number of beam crossings are going to be averaged out. Therefore it is a gradual change in time almost proportional to the instantaneous luminosity. Luminosity leveling scheme again helps to minimize this effect.

5.5. *Long term stability*

In Run II, the Tevatron beam store is not expected to exceed 48 hours. While the data taking is going on with the stored beam, phototube calibration by laser-driven pulsed green light is not going to be performed. Therefore we need to understand the extent of the change of the response in 48 hours.

In general, when the high voltage is turned on, there is a minor overshoot of the response followed by an expopnential-like fall down to normal level[26,27]. Examples of such trend are shown in Fig. 33 in which the relative gain of five tubes are plotted for the initial 90 minutes after the high voltage was turned on.

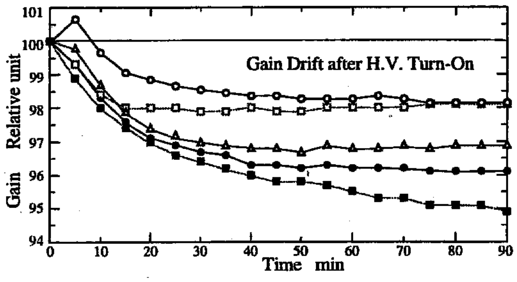

Fig. 33. Examples of exponential-like fall of the response after the intial overshoot at the time of high voltage turn-on. The points are normalized at $t = 0$.

The test described here was designed to quantify the part of gradual change of long time constant, ignoring the initial overshoot which is only an instantaneous phenomenon.

The test sequence is illustrated in Fig. 34. The UV laser was flashed by 15-minute cycle bursts of 100 pulses each at 1 Hz while the background current induced by green LED was sustained at 500 nA continuously. The continuous background current is to mimick the real experimental condition. For every burst the phototube response was averaged. This process continued for 80 hours.

Some examples of the trend over 120 hours are shown in a photo-copy of an arbitrarily chosen data sheet in Fig. 35. In these graphs, the first point at

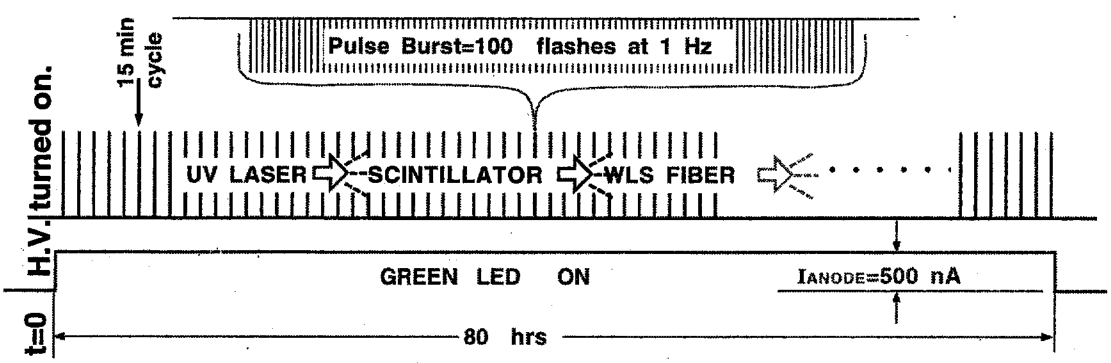

Fig. 34. Light flash sequence for long term stability test.

$t = 0$ is normalized to 1. Since the second point is at 15 minutes, there is a noticeable jump from the first point as expected from the initial rapid change as shown in the examples in the previous figure.

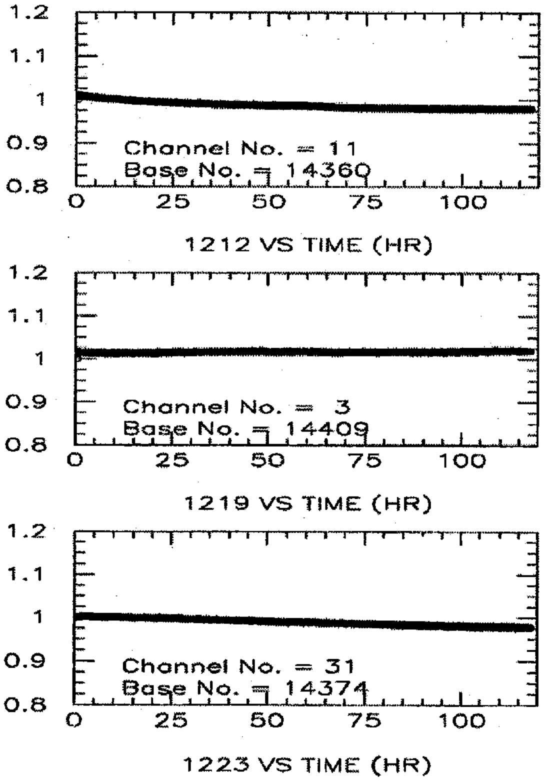

Fig. 35. Examples of the change of the response over 120 hours after high voltage turn-on. The first point at $t = 0$ is normalized to 1.

5.5.1. *Average Drift, Maximum Drift*

Each of the plots of the response over the entire 80 hours period is fitted by a straight line excluding the very firts point at $t = 0$. The slope of the line was defined as "Average Drift" per day.

Another quantity derived from this measurement was "Maximum Drift" per 48 hours. Within any consecutive 48 hour periods, the maximum of the diffrences between the maximum and the minimum points was defined as "Maximum Drift". It is. therefore, almost equivalent to an upper limit of the Average Drift normalized by a factor of two for the difference of the time periods.

Fig. 36 is the plot of the histograms of these two quantities.

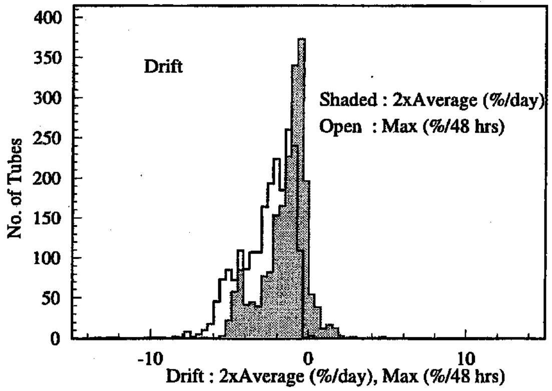

Fig. 36. Distribution of Average Drift and Maximum Drift as defined in the main text. The Average Drift was doubled to compare with Maximum Drift which is calculated for 48 hour period.

In the figure, the horizontal scale of the Average

Drift was doubled to make it equivalent to Maximum Drift of 48-hour basis. As noticed, while the Average Drift, as calculated in % per day, has some tail in the positive side, all tubes are negative in Maximum Drift. Naturally these two quantities are correlated with each other as seen in the scatter plot in Fig. 37.

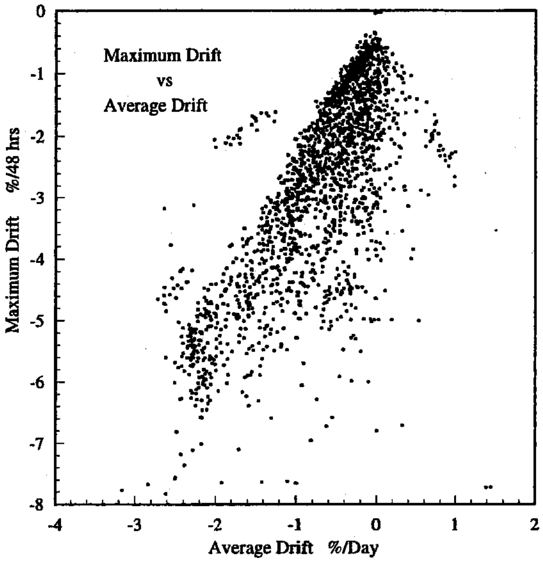

Fig. 37. Scatter plot of Maximum Drift against Average Drift.

44 tubes that exceeded the specified limit of the Maximum Drift, 6 % per 48 hours, were rejected.

5.6. *High voltage turn-on time*

In the data set described above, six of the 2216 tubes showed a small increase in the response in time but all the rest showed decrease. A straight line fit was made to the points beyond 20 hours after turning on the high voltage. The "turn-on time" was defined as the time at which the measured value reachs within 3 % of the straight line extrapolated back to time zero.

94 % of the tubes were less than 10 min in the above defined time. 11 tubes that showed greater than 2 hours were rejected.

5.6.1. *Time to return to normal*

In the actual run, the high voltage of the tubes will be lowered to the standby mode at the time of beam injection into Tevatron, in order to avoid possible exposure to large signals from spurious spray of scraped beam halo. The test was designed to measure how quickly the normal response would be recovered after the high voltage was back to the normal operating voltage from the standby value. The high voltage was lowered to and kept at 100 V for 30 min and then raised to 1100 V. The laser-driven pulsed green light was flashed 100 times at 1 Hz in each of the pulse bursts at 1.5 min interval. After the voltage was back on, "time to return" was defined as the time to return to within less than 2 % of the gain at the previous normal operation. 97 % of the tubes returned to their normal point within 3 min and all 2177 tubes tested returned normal within 10 min. Therefore no tube was rejected on the sole basis of this quantity.

5.7. *Relative quantum efficiency*

To monitor the consistency of the quantum efficiency, 3 tubes were sampled out of every delivered batch of 30 tubes. As mentioned in Section 4.2.3, a dedicated scintillator-tile-fiber set with Ru^{106} was used for this measurement. Using the trigger from a pair of counters, the zero pulse height events were counted. Then, assuming a Poisson distribution, we determined the mean number of p.e.'s which was regarded as the relative quantum efficiency.

Fig. 38 shows the distribution of the measured mean number of p.e.'s. The measured relative quantum efficiency must be related to the cathode luminous sensitivity and/or blue sensitivity. Indeed the scatter plot of the relative quantum efficiency against the luminous sensitivity provided by the manufacturer, shown in Fig. 39, shows the proportionality between these quantities. The line is drawn from the origin using the average of the tube-by-tube ratio of the two quantities.

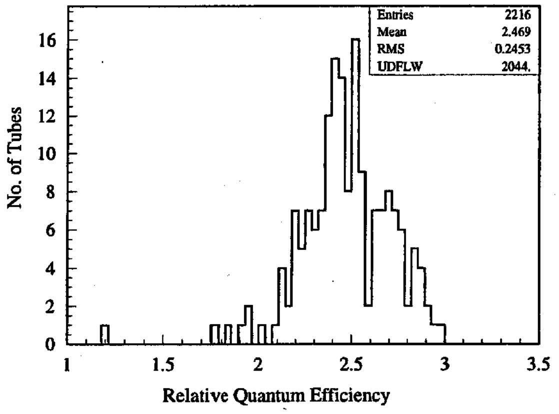

Fig. 38. Distribution of the relative quantum efficiency.

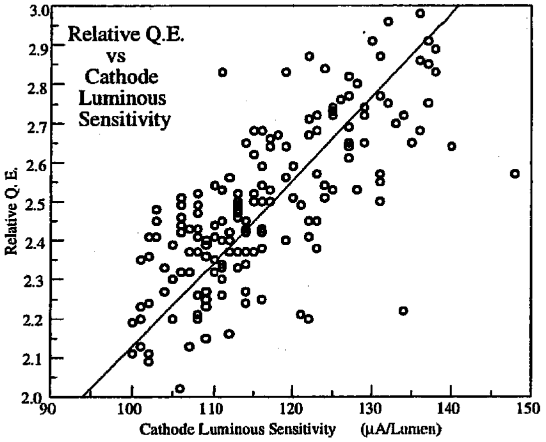

Fig. 39. Scatter plot of the relative quantum efficiency vs. the luminous sensitivity. The line is drawn from the origin with a slope corresponding to the ratio of the average of the two quantities.

6. Dependence of characteristics on manufacturing sequence

We investigated whether there is a dependence of the measured quantities on the order of the tube serial number, assuming that the serial number is in the sequence of the manufacturing. If a gross structure is observed exceeding random fluctuations in a plot, it may indicate that there is room for improvement in the quality by a more rigorous control of the manufacturing process. We plot several of the measured quantities in Figs. 40, 41, and 42.

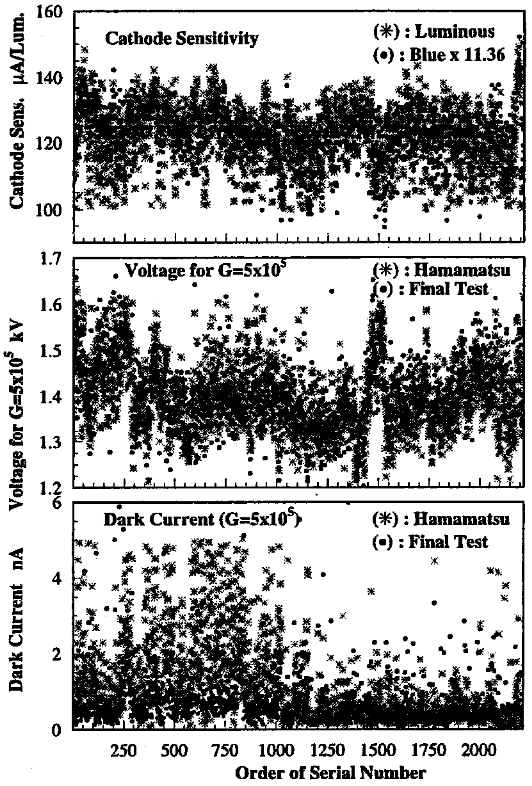

Fig. 40. Dependence of the measured quantities on the sequence of the serial number. Top: cathode luminous sensitivity and blue sensitivity with the latter normalized by a factor of 11.4. Middle: voltage for gain of 5×10^5. Final test data was overlaid with the data from Hamamatsu with a normalization factor of 0.92. Bottom: dark current for gain of 5×10^5. Final test data with the voltage-scaling as described before was overlaid with the data from Hamamatsu.

In Fig. 40, the cathode luminous and blue sensitivity exhibit a gross structure. The voltage for the nominal gain of 5×10^5 also has a gross structure. The plot of the dark current clearly shows much larger fluctuations in the first half of the serial number sequence and it is again obvious that the dark current was maintained below the specified 5 nA by rejecting the tubes that exceeded, whereas the tubes of the second half of the serial number sequence are mostly below 1 nA.

In the case of the peak current for four different

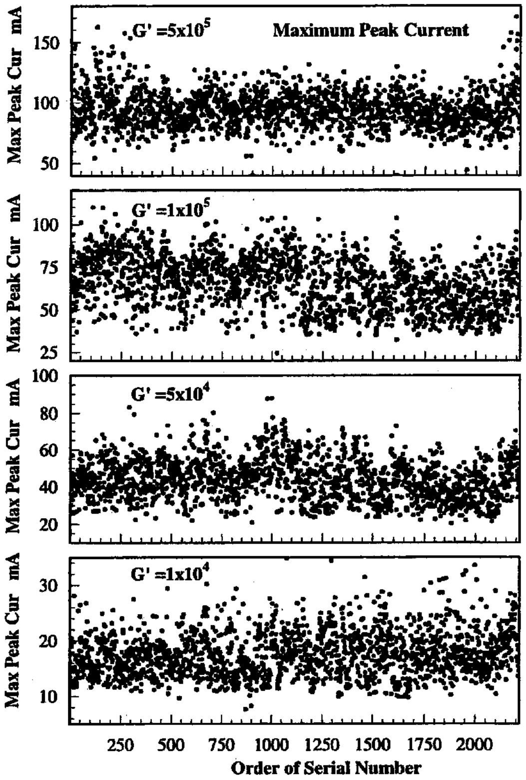

Fig. 41. From top to the bottom, maximum peak current for the relative gain of 5×10^5, 1×10^5, 5×10^4, and 1×10^4 are plotted against the order of the serial number. For the tubes which did not reach the maximum peak current by the limit of the incident-light, the maximum measured current was substituted.

gain values plotted in Fig. 41, gross dependence on the serial number sequence is not obvious beyond random spread. In the Shift and Drift plotted in Fig. 42, a gradual change of the distribution beyond random spread is obvious.

7. Summary of rejected tubes

Out of 2,216 tubes received, 12 tubes were found with a major failure due to cracks developed in the course of delivery or in the early part of the test. Additional 108 tubes were rejected by failing at least one of the specifications. The statistics are listed in Table 9.

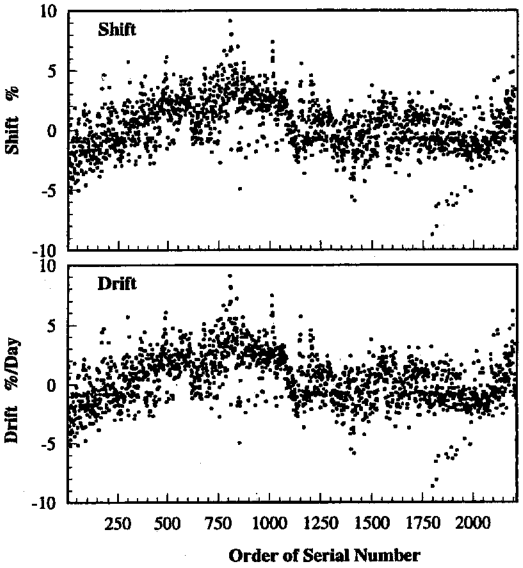

Fig. 42. Shift (top) and drift (bottom) were plotted against the order of the serial number.

Requirement	No. of rejected tubes
Crack/loss of vacuum	12
Dark current ≤5nA	10
|Shift| ≤5 %	49
Drift ≤10 %	14
Max deviation ≤6 %	44
Turn-on time ≤1 hr	14
Time to return ≤10 min	0
Rejected total	120

Table 10
Rejected tubes.

Overlap among the reasons for rejection is rare, and most tubes were rejected for a single reason.

8. Conclusions

We have made extensive measurements of the properties of 2,216 Hamamatsu R4125 photomultiplier tubes used for the upgraded CDF Endplug calorimeter. Some of the major quantities were measured twice.

The measured quantities were :

- relative gain as a function of high voltage;
- dark current;
- linearity;
- stability in time;
- stability against background current fluctuation;
- relative quantum efficiency (for smaller ensemble of sampled tubes).

From our systematic study on thye large number of tubes, we can draw the following conclusions:

- Quantities measured twice were generally in good agreement. Especially the agreement of the relative gain as a function of the voltage was excellent between two measurements.
- Relative gain derived from the spread of the anode pulse height distribution was in good agreement with the true gain from single p.e. peak measurement multiplied with the expected factor of ~1.2 .
- The ratio between the relative gain we measured and the gain measured by the manufacturer as the anode-cathode current ratio is much greater than the expected value calculated from the nominal parameters of the phototube. A supplemental data provided by Hamamatsu indicated that there was a normalization error in the anode-cathode current ratio measurement.
- However there is a strong correlation between the gain measured by the manufacturer and our measurement and the gain, and conversely the voltage for a certain gain, can be well normalized by a factor common to all tubes.
- Among the quantities measured twice, only Shift was significantly affected by the conditioning process inserted between the two test sequences.
- The tubes show small variations of the major characteristics independent of the production date over a two year period.
- The distribution of the properties are well clustered with small tails and our original selection criteria were all well justified.
- Some of the characteristics exhibit a gross structure in plots against the serial number sequence indicating possibilities of further improvement by better quality control in manufacturing.
- 5.4 % of the tubes failed at least one of our selection criteria.
- The largest number of rejected tubes was with regard to the Shift of the gain due to background current change and the maximum drift. These characteristics need attention towards further improvement of the phototubes.

9. ACKNOWLEDGEMENTS

We greatly owe to K. Hara for performing supplemental measurements and for numerous valuable discussions. J. M. Houptman and A. D. Russell are gratefully acknowledged for reading the manuscript and making valuable comments and corrections. This work was a part of the CDF Endplug Calorimeter Upgrade project and the contribution of the members of the project in various aspects of this work is greatly appreciated. We thank the Fermilab staff and the technical staffs of the participating institutions for their vital contributions.

This work was supported by the U.S. Department of Energy and National Science Foundation; the Italian Istituto Nazionale di Fisica Nucleare; the Ministry of Education, Science and Culture of Japan; the Natural Sciences and Engineering Research Council of Canada; the National Science Council of the Republic of China; the A. P. Sloan Foundation; and the Swiss National Science Foundation.

10. APPENDIX

Relative gain measurement[30,31,27]

In our measurement, the average number of photons μ_{ph} incident on the photocathode was kept constant. Therefore the pulse-by-pulse number of photons N_{ph} has a Poisson distribution around the mean value μ_{ph}:

$$P(N_{ph}) = Poisson(N_{ph}, \mu_{ph}) . \qquad (25)$$

Since the process of photo-electron emission from the photocathode is a binomial process with quantum efficiency ε_Q as the probability, the number of p.e. $N'_{p.e.}$ is a convolution of a binomial function with the above Poisson distribution of the incident photons. The result is a Poisson distribution:

$$\begin{aligned} \mathit{emitted\,p.e.}\ &: \\ P(N_{p.e.}) \ &= \sum_{N_{ph}=N_{p.e.},N_{p.e.}+1,\cdots}^{\infty} \\ &\quad \mathit{Binomial}(N_{p.e.}, \varepsilon_Q \cdot N_{ph}) \cdot \mathit{Poisson}(N_{ph}, \mu_{ph}) \\ &\quad = \mathit{Poisson}(N_{p.e.}, \varepsilon_Q \cdot \mu_{ph}) \end{aligned} \tag{26}$$

around a mean value

$$\mu_{p.e.} = \varepsilon_Q \cdot \mu_{ph} \ . \tag{27}$$

The emitted p.e.'s go through another binomial process before reaching the first dynode because the electron collection efficiency, ε_K^{D1}, of the first dynode is less than 100 %. Therefore one needs another convolution of the binomial distribution and the Poisson distribution of the emitted p.e.'s in the above to obtain the number $N_{p.e.}^{D1}$ of p.e.'s that *survived* and hit the first dynode. By the same argument as in the above, the result is a Poisson distribution:

$$\begin{aligned} &\mathit{p.e.'s\ survived\ to}\ D_1\ : \\ &\quad P(N_{p.e.}^{D1}) \ = \ \mathit{Poisson}(N_{p.e.}^{D1}, \varepsilon_K^{D1} \cdot \mu_{p.e.}) \ . \end{aligned} \tag{28}$$

The mean value is now $\varepsilon_K^{D1} \cdot \mu_{p.e.}$.

The number of secondary electrons N_1 emitted from the first dynode with a secondary emission ratio Δ_1 is a convolution of a Poisson distribution around a mean $\Delta_1 \cdot N_{p.e.}$ with the Poisson distribution of the $N_{p.e.}^{D1}$ derived above. With the same argument as for deriving Eq. 28 from Eq. 26, N_1 can be replaced by N_1^{D2} as the number of electrons emitted from the first dynode and survived to the second dynode, even though the electron collection efficiency of the second and the higher dynodes are expected to be close to 100%.

$$\begin{aligned} &\mathit{emitted\ from\ 1st\ Dynode}\ : \\ &P(N_1^{D2}) = \sum_{N_{p.e.}^{D1}=1,2,\cdots}^{\infty} \\ &\qquad \mathit{Poisson}(N_1^{D2}, \Delta_1 \cdot N_{p.e.}^{D1}) \\ &\qquad \cdot \mathit{Poisson}(N_{p.e.}^{D1}, \varepsilon_K^{D1} \cdot \mu_{p.e.}) \ . \end{aligned} \tag{29}$$

Δ_1, though not explicitly noted, is therefore a product of the secondary emission ratio of the first dynode and the electron collection efficiency of the second dynode.

Cascading the secondary electron emission process down to the anode, one can extend the above equation to the distribution of the electrons from the anode as:

$$\begin{aligned} P(N_A) \ = \ &\sum_{N_9^{D10}=1,,..}^{\infty} \ \sum_{N_8^{D9}=1,,..}^{\infty} \cdots \sum_{N_1^{D2}=1,,..}^{\infty} \ \sum_{N_{p.e.}^{D1}=1,,..}^{\infty} \\ &\mathit{Poisson}(N_{10}^{A}, \Delta_{10} \cdot N_9^{D10}) \\ &\cdot \mathit{Poisson}(N_9^{D10}, \Delta_9 \cdot N_8^{D9}) \\ &\cdots \\ &\cdot \mathit{Poisson}(N_1^{D2}, \Delta_1 \cdot N_{p.e.}^{D1}) \\ &\cdot \mathit{Poisson}(N_{p.e.}^{D1}, \varepsilon_K^{D1} \cdot \mu_{p.e.}) \ . \end{aligned} \tag{30}$$

Analogous to $N_{p.e.}^{D1}$ and N_1^{D2} in Eq. 29, N_i^{Di+1} is the number of electrons emitted from the i-th dynode and survived to the next dynode, and Δ_i is the secondary electron emission ratio of the i-th dynode times the electron collection efficiency of the next dynode. Similarly N_{D10}^{A} is the number of electrons that reached at the anode. It should be noted that, due to the nature of the binomial processes, the statistical fluctuation of the number of incident photons and the number of emitted p.e. are absorbed into the fluctuation of the p.e. that survived to the first dynode.

The mean numbers of electrons are:

$$\mu_{p.e.}^{D1} \ = \ \varepsilon_K^{D1} \cdot \mu_{p.e.} \tag{31}$$

for the p.e.'s that reached the first dynode, and

$$\mu_i \ = \ \Delta_i \Delta_{i-1} \cdots \Delta_1 \cdot \varepsilon_K^{D1} \cdot \mu_{p.e.} \tag{32}$$

for the electrons emitted from the i-th dynode and reached the next dynode.

From the above, the relative variance of the anode signal σ_A/μ_A can be expressed by a quadratic sum of the relative variances as follows:

$$\left(\frac{\sigma_A}{\mu_A}\right)^2 = \left(\frac{\sigma_{p.e.}^{D1}}{\mu_{p.e.}^{D1}}\right)^2 + \left(\frac{\sigma_1}{\mu_1}\right)^2 + \cdots + \left(\frac{\sigma_{10}}{\mu_{10}}\right)^2 , \tag{33}$$

where σ_i is the variance of μ_i. Corresponding to each Poisson distribution, the variance σ_i is $\sqrt{\mu_i}$.

Therefore the above equation leads to:

$$\left(\frac{\sigma_A}{\mu_A}\right)^2 = \frac{f}{\mu_{p.e.}^{D1}}\,, \tag{34}$$

with f defined as:

$$f \equiv \left(1+\frac{1}{\Delta_1}+..+\frac{1}{\Delta_1\Delta_2..\Delta_{10}}\right). \tag{35}$$

From the above, the relative gain G' defined as:

$$G' \equiv \frac{{\sigma_A}^2}{\mu_A} \tag{36}$$

can be expressed as a function of the interstage gains of the dynodes as:

$$G' = f\cdot G\,, \tag{37}$$

where the true gain G, the gain of the electron multiplication process, is defined as:

$$G \equiv \frac{\mu_A}{\mu_{p.e.}^{D1}}\,. \tag{38}$$

Therefore G' is greater than G by a factor f.

Larger the gain, diminish the second and the higher terms of f.

If the secondary emission ratio is the same, Δ, for all dynodes, f can be a simpler form in good approximation [13]:

$$f = \frac{\Delta}{\Delta-1}. \tag{39}$$

If the gain was measured as the ratio of the anode output current I_A to the current flown into the photocathode I_K as:

$$G_{A/K} \equiv \frac{I_A}{I_K}\,, \tag{40}$$

it is equivalent to the ratio of the μ_A and $\mu_{p.e.}$:

$$G_{A/K} = \frac{\mu_A}{\mu_{p.e.}}\,. \tag{41}$$

Therefore using the relationship of Eq. 31:

$$G_{A/K} = \varepsilon_K^{D1}\cdot G\,. \tag{42}$$

This is the gain the manufacturer measured. Therefore the ratio between the relative gain and the gain measured by the manufacturer is supposed to be:

$$\frac{G'}{G_{A/K}} = \frac{f}{\varepsilon_K^{D1}}\,. \tag{43}$$

In the above, a simplistic assumption was made that ε_Q, ε_K^{D1}, and Δ_i are all constant pulse-to-pulse without spread. Any spread due to local non-uniformity will add up to the spread of the anode signal distribution. However, in the later stages of the electron multiplication, the effect of such non-uniformity is almost constant pulse to pulse due to the large number of the involved electrons spread over effective area and therefore it should not contribute to the spread of the distribution of the secondary electrons. Most likely, in the first few dynodes where the number of electrons is not large, there could be an effect. To minimize the effect, it is plausible to use a large number of incident photons and a large gain within the limit of saturation.

References

[1] L. Balka *et al.*, Nucl. Instr. Meth. A 267 (1988) 272.

[2] S. Bertolucci *et al.*, Nucl. Instr. Meth. A 267 (1988) 301.

[3] The CDF collaboration, *The CDF II Detector Technical Design Report*, Fermilab-Pub-96/390-E CDF (1996); C. Newman-Holmes, Nuclear Physics B (Proc. Suppl.) 44 (1995) 20, *Proceedings of 4th International Conference on Advanced Technology and Particle Physics*, Como, Italy, 1994.

[4] *Run II Handbook*, http:/www-bd.fnal.gov/runII/index.html.

[5] Y. Fuki *et al.*, Nucl. Instr. Meth. A 267 (1988) 280.

[6] G. Brandenburg *et al.*, Nucl. Instr. Meth. A 267 (1988) 257; S. Cihangir *et al.*, Nucl. Instr. Meth. A 267 (1988) 249.

[7] M. G. Albrow *et al.*, Nucl. Instr. Meth. A 258 (1987) 23.

[8] G. W. Foster, J. Freeman, and R. Hagstrom, Nucl. Phys. B (Proc. Suppl.) 23A (1991) 92.

[9] G. Apollinari, P. de Barbaro, and M. Mishina, *Proceedings of IV International Conference on the Calorimetry in High Energy Physics*, La Biodola, Elba, 1993, p 200.

[10] T. Asakawa *et al.*, Nucl. Instr. Meth. A 452 (2000) 67; M. Albrow *et. al.*, Nucl. Instr. Meth. A 431 (1999) 104.

[11] G. Apollinari *et al.*, Nucl. Instr. Meth. A 412 (1998) 515; G. Apollinari and A. Solodsky, CDF Note No. 4489 (2000).

---

[13]

$$1+\frac{1}{\Delta_1}+\frac{1}{\Delta_2}+\cdots+\frac{1}{\Delta_{10}} \approx \sum_{i=0,1,..}^{\infty}\frac{1}{\Delta_i} = \frac{\Delta}{\Delta-1}\ :\ (\Delta_i \equiv \Delta\ >\ 1)$$

[12] S. Aota *et al.*, Nucl. Instr. Meth. A 352 (1995) 557; S. Aota *et. al.*, Nucl. Instr. Meth. A 420 (1999) 48.

[13] P. de Barbaro *et al.*, CDF Note. No. 2545 (1994).

[14] *Kuraray scintillator catalog*, Methacrylic Resin Division, Kuraray Co. Ltd. Tokyo, Japan.

[15] S. Aota *et al.*, Nucl. Instr. Meth. A 357 (1995) 71.

[16] D. Cauz *et al.*, CDF Note No. 3827 (1996); D. Cauz, Internatl. J. Modern Physics 16 (2001) 1126.

[17] J.Strait and D.C. Lewis, CDF Note No. 1854 (1992).

[18] G. Apollinari and W. Koska, Fermilab Internal Note TS-DET 95-006 (1995); CDF Plug Upgrade Photomultiplier Tube Subgroup, CDF Run II Technical Design Report (1996).

[19] P. Chang and V. Papadimitriou, CDF Note. No 3646 (1997).

[20] R. Wigmans, Nucl. Instr. Meth. A 259 (1987) 389.

[21] M. Albrow *et al.*, CDF Note No. 5545 (2001). Nucl. Instr. Meth. A 480 (2002) 524.

[22] G. Apollinari *et al.*, CDF Note No. 4142 (1997).

[23] K. Hara, S. Kim, and K. Takikawa, Proceedings 1996 DPF/DPB Summer Study, "New Directions for High Energy Physics", Snowmass, Co.,1996.

[24] R.J. Yaremna *et al.*, IEEE Trans. on Nuclear Science, Vol 4 (1993) p750; R.J. Yarema *et al.*, *Presented at 6th Pisa Meeting on Advanced Detectors*, La Biodola, Isola d'Elba, 1994. Italy.

[25] W. Koska *et al.*, Nucl. Instr. Meth. A 406 (1998) 103.

[26] Information given by Hamamatsu Photonics.

[27] Hamamatsu Phtonics KK. "Photomultiplier Tube : Principle to Application"

[28] M. Gallinaro *et al.* CDF Note No. 1839 (1992).

[29] T. Devlin *et al.*, Nucl. Instr. Meth. A 268 (1988) 24.

[30] J. Rademacker, Nucl. Instr. Meth. A 484 (2002) 432.

[31] G. F. Knoll, "Radiation Detector and Measurement, Second Edition", John Willey & Sons, (1988) p259.

[32] K. Hara, Private communication.

[33] Hamamatsu Photonics, Private communication

[34] I. Fiori, *et. al.*, CDF Note No. 1840.